SPECIFICATION AND MODELING OF MID-SPATIAL FREQUENCY ERRORS IN OPTICAL SYSTEMS

by

Luke DeMars

A dissertation submitted to the faculty of
The University of North Carolina at Charlotte
in partial fulfillment of the requirements
for the degree of Doctor of Philosophy in
Optical Science and Engineering

Charlotte

2023

Approved by:

Dr. Thomas Suleski

Dr. Glenn Boreman

Dr. Gregory Gbur

Dr. Angela Davies Allen

Dr. Brigid Mullany

ABSTRACT

LUKE DEMARS. Specification and modeling of mid-spatial frequency errors in optical systems. (Under the direction of DR. THOMAS J. SULESKI)

Recent advancements in manufacturing and post-processing of optics with sub-aperture methods have enabled greater degrees of freedom to realize complex optical surfaces. Introduction of residual mid-spatial frequency (MSF) surface errors is a consequence of sub-aperture manufacturing. MSF errors have spatial frequencies between ‘low frequency’ form and ‘high frequency’ roughness with ambiguous bounds and with distributions that range from nearly random to highly deterministic and complex, depending on manufacturing method and conditions. MSF errors degrade optical performance and present significant challenges for both specification and optical performance predictions. The lack of specifications that directly connect to optical performance and the lack of widely available capabilities and procedures for modeling of generalized MSF errors are significant impediments to understanding their impacts in imaging systems.

The primary goals of this dissertation are (1) to explore and expand the connections between MSF specifications and optical performance for complex MSF error distributions, and (2) to demonstrate the implementation of these concepts within commercial software packages to enable the exploration of generalized MSF errors in optical systems. Results are addressed through three articles. The first article addresses the mathematical development and benefits of pupil-difference probability distribution (PDPD) moments to specify MSF errors and connect them to optical performance. The second article builds from this work to provide modeling procedures and explores their application to both random and deterministic MSF errors. The third article demonstrates the integration of these new concepts and methods into MATLAB™ and CODE V™, and their use on sample refractive and reflective imaging systems.

DEDICATION

To my good friend Ruach “Dabul” Wal, for instilling drive, curiosity, and patience in me. Thank you for the laughs, lessons, and memories. You are missed dearly.

ACKNOWLEDGEMENTS

I would like to express my gratitude to my advisor, Prof. Thomas J. Suleski, for his continuous guidance and helping hand in my academic journey. I genuinely appreciate your hard work and for always being there to answer or assist with any questions. I would also like to convey my gratefulness to my committee members for the time and effort they have given in reviewing this body of work and for helpful discussion and suggestions.

I want to extend my thanks to my labmates: Dr. Sara Moein, Dr. Shohreh Shadalou, and Santiago Rueda Para. I appreciate all the technical conversations, advice, and friendship you all provided during our time together. I would also like to thank Prof. Jannick Rolland (Univ. of Rochester), Dr. Aaron Bauer (Univ. of Rochester), Yiwen Fan (Univ. of Rochester), Prof. Miguel Alonso (Aix Marseille Univ. & Univ. of Rochester), Prof. Greg Forbes (Macquarie Univ.), and Dr. Bryan Stone (Synopsys) for their valuable input and collaboration. In addition, I would like to thank Dr. Liangyu He, whose area structure function software I built on to calculate the pupil-difference moment maps used extensively throughout this dissertation.

Last but not least, I would like to thank my family and friends, who have contributed to my academic endeavors in many ways.

This work was funded through the Center for Freeform Optics, the NC ROI Consortium for Self-Aware Machining and Metrology, UNC Charlotte’s GASP/Fellowship, and UNC Charlotte’s GSSF summer funding.

TABLE OF CONTENTS

CHAPTER 1: INTRODUCTION

CHAPTER 2: PUPIL-DIFFERNCE MOMEMENTS FOR ESTIMATING RELATIVE MODULATION FROM GENERAL MID-SPATIAL FREQUENCY SURFACE ERRORS

CHAPTER 3: ON THE USE OF PUPIL-DIFFERENCE MOMENTS FOR PREDICTING OPTICAL PERFORMANCE IMPACTS OF GENERALIZED MSF SURFACE ERRORS

CHAPTER 5: CONCLUSION

LIST OF TABLES

LIST OF FIGURES

LIST OF ABBREVIATIONS

1D	One Dimensional
2D	Two Dimensional
AB	Aberrated
ASF	Area Structure Function
BSP	Beam Synthesis Propagation
DL	Diffraction Limited
EXP	Exit Pupil
INT	Interferogram
MMC	Minimum Modulation Curve
MSF	Mid-Spatial Frequency
MTF	Modulation Transfer Function
NA	Numerical Aperture
NSE	Normalized Standard Error
OTF	Optical Transfer Function
PDPD	Pupil-Difference Probability Distribution
PMMA	Polymethylmethacrylate
PSD	Power Spectral Density
PSF	Point Spread Function
PV	Peak to Valley
RDF	Rapidly Decaying Fourier Series
RMS	Root-Mean-Square

CHAPTER 1: INTRODUCTION

1.1 Background and Motivation: Mid-Spatial Frequency Surface Errors and Impacts on Optical Performance

Sub-aperture manufacturing has enabled the development of compact freeform systems that provide novel functionalities in imaging and non-imaging applications [1]. Mid-spatial frequency (MSF) surface errors are by-products of sub-aperture manufacturing processes that fall between form and roughness [2]. There are several different definitions for MSF surface errors based, for example, on period [3] and spatial frequency [4], residual error after fitting the first 36 fringe Zernike terms [2], Fresnel length [2], and location of diffracted light outside the core of the point spread function [5]. However, these definitions do not consider the optical footprint of the part [6] or the distribution of the MSF surface error [7–10].

Standard MSF distributions include raster, radial, or azimuthal distributions, as shown in Figure 1-1 (a-c) [2]. While the standard distributions cover relevant cases, MSF distributions can be considerably more complex, such as a superposition of the distribution classes over a broad range of mid-spatial frequencies [11,12], as shown in Figure 1-1 (d).

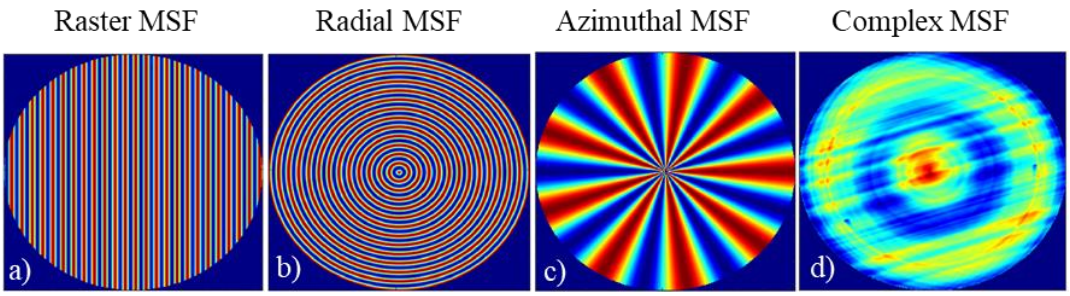

Figure 1-1: (a-c) Representative idealized MSF signatures. (d) Experimentally measured surface that contains a superposition of raster and radial MSF errors.

The complexity of MSF surface errors arises from multiple sources in sub-aperture manufacturing, including the toolpath, tool geometry and wear, vibration, thermal errors, and material [1,13–15]. Considerable efforts have been made to mitigate MSF errors by post polishing [16–21] or random tool paths [22–30] while other methodologies focus either on non-contact processing methods or tool design optimization [31].

Efforts to understand and prevent MSF errors in sub-aperture manufacturing have been made because these errors have a variety of impacts on optical performance, including image degradation [6,32,33], ghost images [34], low-angle scattering [5,35], self-imaging [36,37], distortion [38,39], and reflectivity in the x-ray regime [40]. Previous methods for performance prediction of imaging systems with MSF surface errors have assumed random or isotropic error distributions [5,41,42]. This assumption of randomness has presented a challenge for the specification of generalized MSF errors and their connections to optical performance, as MSF errors with similar single valued statistics can have drastically different optical performances [7,9,10,43]. To illustrate this challenge, two MSF surface errors, each with the same root mean square (RMS) surface error of 70 nm and peak to valley (PV) of 200 nm, have been superimposed onto identical but separate BK7 planoconvex lenses with the same focal length of 100 mm. We then use the 2D image simulation tool in CODE V™ [44] to simulate the image of a USAF bar target at a source wavelength of 546 nm, as shown in Figure 1-2. Figure 1-2 shows that, although both MSF errors have the same specifications, they have different imaging performance. The difference can be seen in the directionality of the degradation in the 2D modulation transfer function (MTF) in each case. For the radial MSF distribution, the 2D MTF has radially symmetric degradation which produces a halo blur in its image. For the raster MSF distribution however, the 2D MTF degradation is in the direction of the surface error, which produces duplicate images as previously described by Tamkin [34].

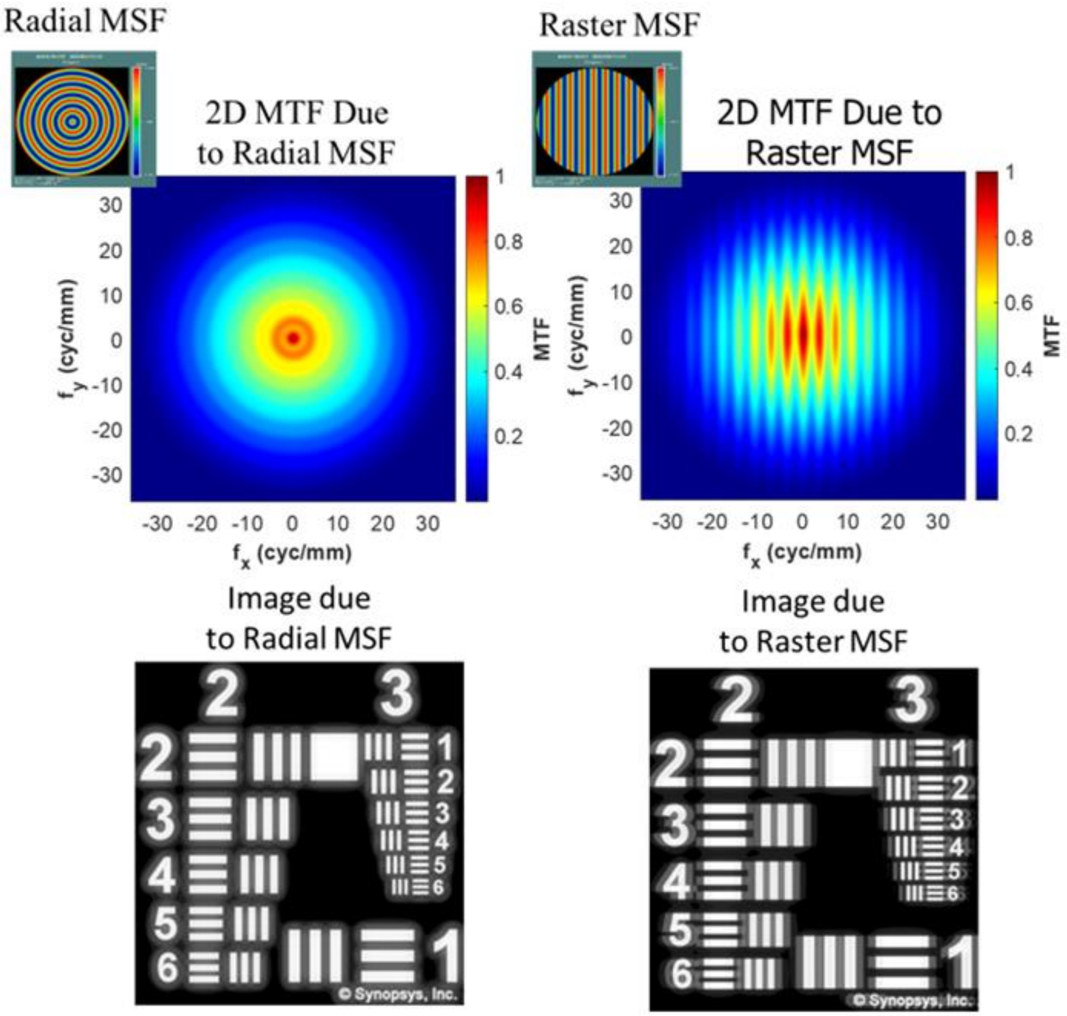

Figure 1-2: Comparison of imaging from lens elements with MSF errors that have different distributions but similar statistics.

Progress has been limited in specification and modeling of generalized MSF surface errors due to the assumption of isotropic or radial MSF surface errors and a lack of commercially available software and procedures to model generalized MSF surface errors in imaging systems. With this in mind, this dissertation addresses these challenges by first exploring use of novel areal specification methods that facilitate differentiation of the performance impacts of different MSF error distributions. A workflow is then developed and implemented in commercial software packages to demonstrate use of these areal specifications to assess the impacts of generalized MSF errors at a system level.

1.2 Review: Areal Specification

The general goal of areal specification is to quantify complex distributions where one-dimensional specification tools and metrics would leave ambiguity [9,45,46]. Historically, three primary methods of areal specification have been used: areal power spectral density (PSD), orthogonal decomposition, and the area structure function (ASF). We now briefly review these three methods and their limitations below.

The areal PSD is a 2D plot that quantifies the normalized Fourier magnitude squared as a function of spatial frequency [46] and has been utilized in both cartesian [47–49] and polar formats [11,50–53]. A main benefit of using the areal PSD is that it can distinguish between different MSF distributions [11]. However, the primary quantifiable metric obtained from the areal PSD is the RMS of the surface error [54]; phase information is lost from taking the modulus during calculation of the areal PSD. It is also possible to determine the RMS slope, curvature, and shape parameters [55]. While the RMS slope has previously been used for specifying MSF errors [40,56,57], the curvature and shape parameters have been under-utilized. One recent approach proposed stitching together the amplitude and phase of multiple 2D Fourier transforms of height maps of increasingly higher resolutions. The inverse Fourier transform of the 2D stitched spectra is then taken to construct a highly resolved height map [53]. However, no further analysis or use of the highly resolved surface was proposed after reconstruction.

Orthogonal decomposition has also been used to specify MSF surface errors by decomposing the surface error into a weighted sum of orthogonal polynomials. The weighting coefficients of the individual polynomials in the basis set can be visually represented with a two-dimensional 'coefficient map' [58] that can facilitate the identification of different MSF distributions. This method has previously been applied, for example, for circular surfaces using sag orthogonal [59,60] and slope orthogonal basis sets [49,61], for square apertures with sag orthogonal basis sets [48,62], and for more general aperture surfaces using basis sets that have both global and local properties [63–66]. MSF specification using orthogonal decomposition can require tens of thousands of terms to adequately quantify the MSF surface errors.

Lastly, the ASF is a 2D map of height difference variance across a surface aperture [67]. The ASF is an adaption of the structure function, which originated in turbulence modeling [68]. A benefit of the ASF is that it can assess non-stationary surfaces which is relevant for the analysis of both form and MSF errors [67]. Researchers have also shown that the ASF can be stitched together from multiple instruments and can quantify the impacts of the metrology platform instrument transfer function (ITF) on the surface [69]. A limitation of the ASF is its lack of connection to optical performance. Liang and Alonso showed that the ASF can be utilized in a transfer function under the assumption of Gaussian statistics [70], but MSF errors do not necessarily follow Gaussian statistics [10]. In this dissertation, we introduce the pupil-difference probability distribution (PDPD) moments, which are related to the ASF but are a generalization of the height difference moments [10], and show their connections to optical performance.

1.3 Challenges with Optical Modeling of MSF surface errors

Historically, three main approaches have been used for modeling the optical performance of MSF surface errors. The first uses perturbation theory [42,71,72] and statistical optics [73]. Perturbation theory assumes that the amplitude of the perturbation of the alignment or surface of an optic is small enough to approximate the optical path length of the perturbation as the difference in path lengths between the nominal system and the system with the perturbation. This approach has been used in previous work that investigated the impact of tilt, displacement, and form errors [71,72]. Youngworth and Stone were the first to use perturbation theory to project MSF errors through an optical system to its exit pupil [42]. With the resulting error distribution in the exit pupil, they then estimated the optical performance degradation resulting from the MSF error using a simple relationship between the wavefront variance and the Strehl ratio. In recent work, Liang and Alonso explored the validity of perturbation theory in two [74] and three [75] dimensions and found that its validity depends on the distance between the MSF surface error and the plane of propagation, the nominal period of the MSF surface error, and whether or not the MSF surface error resulted in the formation of Talbot images [74,75]. However, even though these ‘rules of thumb’ were explored for generalized low to high NA systems, they have not been explored for specific optical systems up to this point.

Another historical approach to modeling MSF surface errors utilizes statistical transfer functions. A statistical transfer function is a multiplicative factor to the nominal optical transfer function (OTF) of a system and is parameterized by both RMS wavefront error and the autocorrelation of the wavefront [76]. Use of the statistical transfer function has evolved from both turbulence modeling [73,77,78] and surface scatter theory [79,80]. Use of the statistical transfer function for estimating performance degradation due to MSF has previously been proposed by Noll [41] and Harvey [5,81]. While the added parameter of the autocorrelation function is useful for estimating the performance impacts of correlated surfaces, an assumption of Gaussian surface statistics is made in the formulation of the transfer function. As a result, the estimates of performance impacts may not be accurate for generalized MSF errors as they do not always abide by Gaussian statistics [10].

Another method commonly used to model MSF surface errors uses a *phase skin* superimposed onto a nominal surface; the MSF surface error can be thought of as a shallow conformal grating [6,32]. This approach has been applied to both synthesized [6,14,32,33,36,39,70,82–85] and experimentally-measured surface height maps [34,64,86–89]. While methods to superimpose MSF errors onto optical surfaces and apply ray-based and wave-based propagation exist [6,32,34,36,64,87,90,91], previous works have utilized phase skins under three assumptions: (1) the phase skin is superimposed onto a single element that is at the aperture stop [83,86,88,89], (2) the workflow for the phase skins assume radially symmetric or random MSF surface errors [64,84,87], or (3) the pre-processing of the phase skin does not address decomposition of the MSF error distribution [6,32,34], which can be of importance as complex MSF errors may be composed of multiple basic signatures. In this work, we also utilize phase skins to superimpose experimental MSF signatures onto surfaces in optical imaging system. However, unlike previous approaches, this work also adds capabilities to identify and decompose complex MSF distributions without assumption of the surface statistics or symmetry.

A more recent approach for optical modeling of MSF errors uses the Wigner function. This approach enables the propagation of the partially coherent light through an optical system with MSF errors. The cost of using this method is an increase in computation time and the added complexity of multidimensional analysis [35]. This approach has previously been utilized with 1D MSF error cross-sections [35]. It has been suggested this approach can be extended to 2D MSF surfaces, but this would further increase the challenges.

The overall challenge of optical modeling of MSF surface errors is that, due to the lack of general procedures and availability of such procedures in commercial software, there have been limited studies of MSF impacts in imaging systems without the assumptions or complications of previous methods.

1.4 Dissertation Outline

Chapter 2 introduces the concept of PDPD moments, which are multidimensional probability distributions that quantify the height or phase difference of a surface or exit pupil to spatial coordinates and image space spatial frequencies and is used to quantify the relative modulation of an imaging system. We show that the PDPD moments have several advantages for quantifying the optical performance impacts resulting from generalized MSF surface errors.

Chapter 3 builds on use of the PDPD moments and demonstrates their application to predicting optical performance for both random and deterministic MSF errors. Performance estimates for random surfaces made from the generalized method using PDPD moments agree with earlier methods that assumed random surfaces [5,41,42]. We also show a procedure for structured MSF errors to relate the maxima of the PDPD moments to recently introduced performance metrics such as the minimum modulation curve (MMC) [88] and Q', which is the normalized area under the MMC [89]. Finally, we demonstrate the application of these methods to several different MSF error distributions and compare how the estimated optical performance values compare to predictions based on earlier methods that assumed random error distributions.

Chapter 4 demonstrates the integration of MSF modeling and analysis concepts into MATLAB™ and CODE V™, and their application to sample refractive and reflective imaging systems. In addition, we show that the orientation of MSF errors in the system can significantly influence optical performance.

Lastly, Chapter 5 summarizes the results provided in Chapters 2 through 4 and then provides general conclusions on the specification and modeling of MSF surface errors. Finally, suggestions for future research are presented.

CHAPTER 2: PUPIL-DIFFERNCE MOMEMENTS FOR ESTIMATING RELATIVE MODULATION FROM GENERAL MID-SPATIAL FREQUENCY SURFACE ERRORS [10]

2.1 Abstract

Standard surface specifications for mid-spatial frequency errors do not capture complex surface topography and often lose critical information by making simplifying assumptions about surface distribution and statistics. As a result, it is challenging to link surface specifications with optical performance. In this work, we present use of the pupil-difference probability distribution (PDPD) moments to assess general MSF surface errors and show how the PDPD moments relate to the relative modulation.

2.2 Introduction

Sub-aperture tooling is necessary to fabricate optics with freeform prescriptions [1]. Mid-spatial frequency (MSF) surface errors with surface spatial frequencies that fall between form and roughness with unclear boundaries are by-products of sub-aperture manufacturing [2]. Such MSF errors are important to quantify due to their impacts on imaging performance [3]. To quantify these impacts, it is necessary to specify the MSF surface error and connect the specification to an optical performance metric.

Surface specifications for MSF such as the peak to valley (PV), root mean square (RMS) surface error, and RMS slope are simple, single valued specifications, but it has been shown that MSF distributions with similar simple specification values can have significantly different imaging performance [1,4]. One-dimensional specifications, such as the power spectral density (PSD) [5] and structure function [6], have also been used to specify the period and amplitude of the MSF errors present on the surface. However, it has been observed that these 1D representations of MSF can produce similar specifications for different MSF distributions, making it challenging to differentiate the MSF distributions [4,7].

To better assess the entire optical surface, specification tools such as the polar areal power spectral density [8], area structure function (ASF) [9], and orthogonal decomposition [10,11] have been effective in quantifying MSF distributions. Although, the connection between these surface specifications and optical performance metrics that differentiate MSF distributions has not yet been addressed.

Linking surface specification to optical performance has mainly been performed by transfer function [12,13] or perturbative approaches [14,15]. Both approaches have challenges; transfer function approaches are typically based on assumed (e.g., gaussian) surface statistics, while perturbative approaches often lose information about the MSF error distribution by reducing exit pupil metrics to a single-valued quantity (e.g., PV, RMS, RMS slope) for relation to the point spread function (PSF) or modulation transfer function (MTF) [11,14].

We assert that previous methods of connecting MSF surface specifications to optical performance are limited by one or more of the following: (1) the MSF specification makes statistical assumptions that may not hold for deterministic MSF errors; (2) the MSF specifications only consider a portion of the optical surface; or (3) the MSF specification methods may not have direct links to optical performance that differentiate between MSF distributions. All three points must be addressed to facilitate clear connections between optical design, manufacturing, and metrology.

With these statements in mind, Liang and Alonso recently quantified the impacts of general MSF groove structures and their random variations on either an optical surface at the exit pupil [16,17] or by propagating the MSF error from the optical surface to the exit pupil [15]. This work was done by taking the Fourier transform of the pupil-difference probability distribution (PDPD). The PDPD Fourier transform was then multiplied by the diffraction-limited optical transfer function (OTF) to predict optical performance [16,17]. This multiplicative term is also known as the *relative modulation* [18] or, alternately, *Hopkins ratio* [19].

In this previous work, the PDPD was used to make analytical estimates of the relative modulation [16,17]. However, if an analytical solution is not possible, the PDPD becomes challenging to analyze as its probability distribution has four dimensions. For example, if a surface has a standard surface resolution of 1024 x 1024 pixels, then the PDPD will consist of over four million 1D probability distributions.

To reduce the dimensionality in the PDPD without losing connections to optical performance, we propose to utilize the central moments of the PDPD as a function of pupil-shift in an areal map, similar to the area structure function [9]. It should be noted that the area structure function is equivalent to the 2nd moments of the PDPD calculated relative to zero mean. The present work will show the full derivation, and then demonstrate the concept under specific assumptions.

By utilizing the central moments of the PDPD it will be shown that general MSF surface errors can be specified and connected to optical performance. In this work, we first derive the mathematical relationship of the PDPD moments to the relative modulation. We then demonstrate how the PDPD moments address the three main challenges outlined above.

2.3 Relating PDPD moments to Relative Modulation

There are two approaches to formulate the connection between the PDPD moments and the relative modulation. Liang and Alonso proposed the first method, which takes the Fourier transform of the PDPD to calculate the relative modulation [16]. In this paper, we take the complex pupil-difference's weighted average [20] to calculate the relative modulation. We chose the second method to highlight that relative modulation can be calculated without a known PDPD distribution or assumption of stationarity of the PDPD, where stationarity is defined as the case when the PDPD distribution and moments are invariant to pupil-shift [20].

To calculate the relative modulation, we follow the approach of H.H. Hopkins [18] and start with the ratio between the aberrated OTF and the diffraction-limited OTF:

$$M(f_x, f_y)C(f_x, f_y) = \frac{OTF_{AB}(f_x, f_y)}{OTF_{DL}(f_x, f_y)} . \tag{2.1}$$

Here the relative modulation is written as the product of the real part $M(f_x,f_y)$, and a complex factor denoted $C(f_x,f_y)$.

To connect the relative modulation to the pupil difference, we use the autocorrelation definition of the OTF for both the aberrated and diffraction-limited cases [21]:

$$OTF_{DL}(\tau_x, \tau_y) = \frac{\iint P_{DL}(x,y) P_{DL}(x-\tau_x, y-\tau_y)\, dxdy}{\iint dxdy} \tag{2.2}$$

$$OTF_{AB}(\tau_x, \tau_y) = \frac{\iint \exp\left[i(\varphi(x,y) - \varphi(x-\tau_x, y-\tau_y)) \right] dxdy}{\iint dxdy} \tag{2.3}$$

where

$$\tau_i = \lambda f_i z . \tag{2.4}$$

Here P_{DL} represents the diffraction-limited pupil for any general shape, τ_i is the pupil shift, φ is the pupil aberration, λ is the source wavelength, f_i is the image space spatial frequency in the far field, the i subscript denotes x and y vectors, and z is the propagation distance to the image plane from either a single lens or the exit pupil of an imaging system. In addition, we assume the amplitude is constant across the pupil; this is not always the case, but we make this simplification here to focus on analyzing MSF phase errors.

Plugging Eq. (2.2) and (2.3) into Eq. (2.1) and pulling out the mean pupil difference, we obtain the following expression that relates the weighted average of the complex pupil difference to the relative modulation, as shown in Eq. (2.6):

$$M(\tau_x,\tau_y)C(\tau_x,\tau_y) = \exp[i(\overline{PD(\tau_x,\tau_y)})] \times \frac{\iint \exp[i(PD(x,y,\tau_x,\tau_y) - \overline{PD(\tau_x,\tau_y)})]dxdy}{\iint P_{DL}(x,y)P_{DL}(x-\tau_x,y-\tau_y)dxdy} \qquad (2.5)$$

$$= \exp[i(\overline{PD(\tau_x,\tau_y)})]\left\langle \exp[i(PD(x,y,\tau_x,\tau_y) - \overline{PD(\tau_x,\tau_y)})]\right\rangle \qquad (2.6)$$

where

$$PD(x,y,\tau_x,\tau_y) = \varphi(x,y) - \varphi(x-\tau_x,y-\tau_y)\ . \qquad (2.7)$$

This relationship allows us to explore the link between surface specification and optical performance. We start by expanding the relative modulation about its N^{th} central moments in a similar fashion to Hopkins [18],

$$\left\langle H_C^N(\tau_x,\tau_y)\right\rangle = \frac{\iint [(HD(x,y,\tau_x,\tau_y) - \overline{HD(\tau_x,\tau_y)})]^N dxdy}{\iint P_{DL}(x,y)P_{DL}(x-\tau_x,y-\tau_y)dxdy} \qquad (2.8)$$

where

$$HD(x,y,\tau_x,\tau_y) = h(x,y) - h(x-\tau_x,y-\tau_y). \qquad (2.9)$$

Note, in Eq. (2.8), we have factored out the wavenumber (*k*) and the index contrast (Δ*n*) and have left the height distribution (*h*) in the integral. The expansion of the relative modulation is then

$$\begin{aligned} M(\tau_x,\tau_y)C(\tau_x,\tau_y) &= \exp[ik\Delta n(\overline{HD(\tau_x,\tau_y)})](1+ik\Delta n\left\langle H_C^1(\tau_x,\tau_y)\right\rangle \\ &-k^2\Delta n^2\frac{\left\langle H_C^2(\tau_x,\tau_y)\right\rangle}{2!}-ik^3\Delta n^3\frac{\left\langle H_C^3(\tau_x,\tau_y)\right\rangle}{3!}+k^4\Delta n^4\frac{\left\langle H_C^4(\tau_x,\tau_y)\right\rangle}{4!}...). \end{aligned} \tag{2.10}$$

Eq. (2.10) represents the general case, in which the PDPD may be non-symmetric and the relative modulation can have real and complex components. We can make additional assumptions to simplify Eq. (2.10). First, to ensure that the relative modulation is real, we can assume that the underlying PDPD is symmetric [22], which results in zero values for the odd moments. Second, we consider cases resulting in small drops in modulation (~ 0.2 to 0.3), so that higher order moments are negligible. With these simplifications, the relative modulation can be estimated as

$$M(\tau_x,\tau_y)\approx 1-k^2\Delta n^2\frac{\left\langle H_C^2(\tau_x,\tau_y)\right\rangle}{2!}+k^4\Delta n^4\frac{\left\langle H_C^4(\tau_x,\tau_y)\right\rangle}{4!}. \tag{2.11}$$

In Eq. (2.11), the 2nd moment represents the pupil-difference variance, and the 4th moment represents pupil-difference tailedness [23]. The following example considers cases where Eq. (2.11) is valid, but more general examples can be explored using Eq. (2.10).

In Figure 2-1, we visualize calculating the PDPD moments for a raster MSF signature that has ten cycles across the surface, an RMS surface error = 70 nm and a PV = 200 nm. To calculate the 2nd and 4th PDPD moment maps, first a copy of the MSF is made and shifted in increments of τ_x and τ_y. Then the height difference is taken of the MSF and copy at each pupil shift over regions of non-zero overlap. Next, the 2nd and 4th moments are calculated for each pupil difference. Then finally, the moments are placed in the moment map at their respective pupil shift locations.

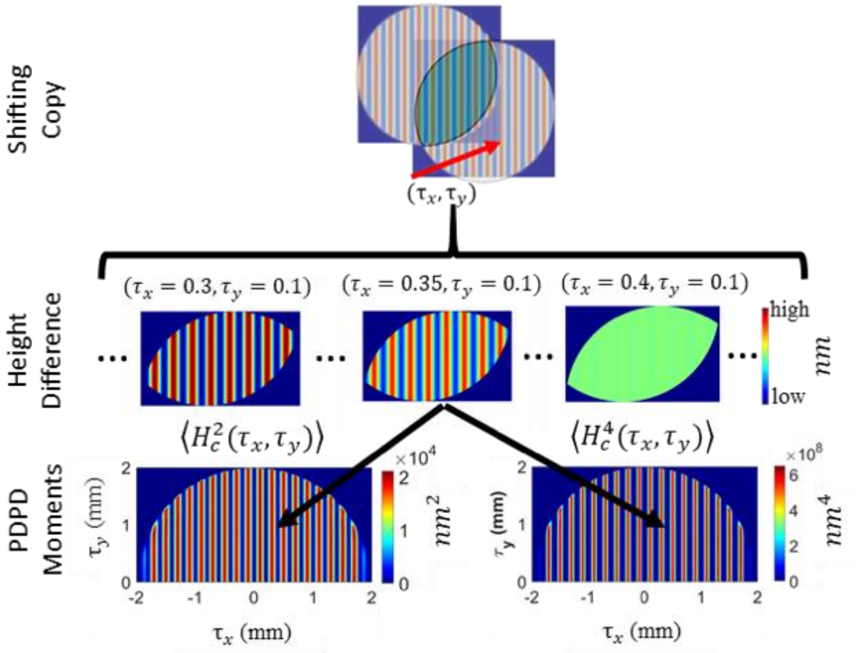

Figure 2-1: Flow diagram of calculating 2nd and 4th PDPD moments of MSF example. [Reprinted] with permission from [10] © Optica Publishing Group.

To conclude this derivation, we emphasize that the estimate in Eq. (2.11) is accurate for symmetric PDPD distributions without assumption of their stationarity. This result, therefore, provides a general relationship that can specify deterministic MSF from sub-aperture manufacturing and connect to optical performance. With the underlying mathematics expressed, we now demonstrate through example how the PDPD moments address the three challenges of specifying MSF and connecting to optical performance.

2.4 Exemplifying Properties of PDPD Moments

First, we show that the PDPD has a non-gaussian distribution and that the PDPD moments fluctuate as a function of pupil shift. This idea is illustrated by assessing three pupil shift locations in the 2nd and 4th moments of the PDPD for the raster sinusoidal MSF surface error shown in Figure

2-1. In Figure 2-2, we show histograms of PDPD distributions at three pupil shifts which represents the half period of the MSF surface error. As the pupil shift increases, in τ_x, the PDPD distribution narrows, and the 2nd and 4th moments decrease, as shown in Table 2-1. The square root of the 2nd moment and the fourth root of the 4th moment are included for comparison to the original surface errors (PV and RMS) in common units. Therefore, this example shows that the PDPD moments can assess general probability distributions without assumption of stationary statistics. In addition, this could be extended to non-stationary surfaces as was done for the area structure function [9].

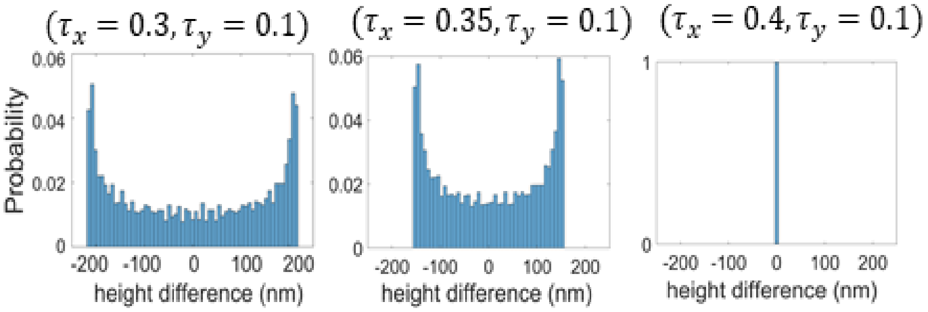

Figure 2-2: Histograms of three pupil shifts of the PDPD for MSF example shown in Figure 2-1. [Reprinted] with permission from [10] © Optica Publishing Group.

Table 2-1: 2nd and 4th PDPD moments of distributions shown in Figure 2-2.

(τ_x,τ_y) (mm)	(0.3,1.0)	(0.35, 1.0)	(0.4, 1.0)
2nd Moment (nm^2)	2.0x10^4	1.0x10^4	3.0
(2nd Moment)$^{1/2}$ (nm)	141.4	100	1.7
4th Moment (nm^4)	6.0x10^8	1.5x10^8	14.0
(4th Moment)$^{1/4}$ (nm)	156.5	110.7	1.9

Next, we consider how the 2nd and 4th PDPD moments assess the entire surface. To do this, we calculate the 2nd and 4th PDPD moments for three characteristic MSF signatures; the raster pattern from Figure 2-1, a radial pattern, and an azimuthal pattern. The radial MSF has ten cycles across the diameter, and the azimuthal MSF has ten cycles around the perimeter. In addition, all three

MSF signatures have an RMS surface error of 70 nm and PV of 200 nm. As shown in Figure 2-3, the maps of the 2nd and 4th moments capture the whole surface MSF distribution and the number of cycles. For example, the PDPD moments calculated from the raster MSF show ten raster oscillations from 0 to 2 mm, the PDPD moments calculated from radial MSF show ten radial oscillations from 0 to 2 mm, and the PDPD moments calculated from azimuthal MSF show ten oscillations across the perimeter. Thus, the PDPD 2nd and 4th moments allow us to differentiate between MSF distributions with similar statistics. This is critical as it has been shown that different MSF distributions with the same RMS and PV can have different optical performance [1,4].

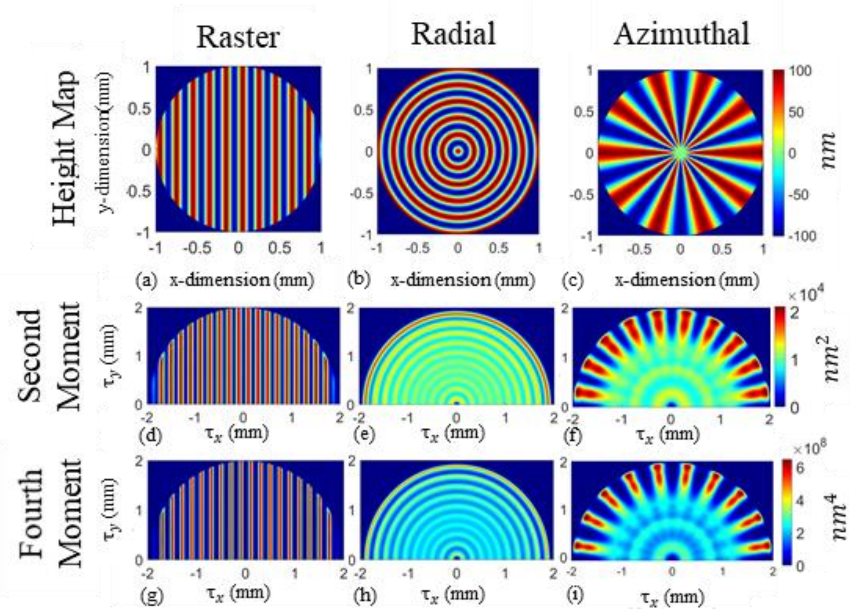

Figure 2-3: Comparison of PDPD second and fourth moments for raster, radial, and azimuthal MSF distributions of similar statistics. Only the top half of the PDPD moment maps are shown to avoid redundancy [9]. [Reprinted] with permission from [10] © Optica Publishing Group.

Finally, we show how to connect MSF surface specification to optical performance. To do so, we use the three MSF examples from Figure 2-3 to calculate the relative modulation in two different ways.

First, we calculate the relative modulation using far-field approximations to calculate the diffraction-limited and aberrated modulation transfer functions (MTF) [24]. To calculate the relative modulation for each aberrated case, we superimpose each MSF error on the curved surface of a plano-convex lens with 100 mm focal length. For this example, we assume the optical surface is at the exit pupil. In addition, we assume an index contrast of $\Delta n = 0.493$ (PMMA in air), a propagation distance $z = 100$ mm, and a source wavelength of $\lambda = 532$ nm. We then propagate the wavefront error to the far field with a Fourier transform, and take the squared modulus of the complex field to calculate the PSF. This process is repeated for a perfect lens (free of MSF errors) to obtain the diffraction-limited MTF. Figure 2-4 shows a qualitative comparison of the PSFs for the aberrated cases. Note that each of the MSF signatures has RMS surface error = 70 nm and PV = 200 nm, and each of the three examples results in a Strehl ratio of 0.84.

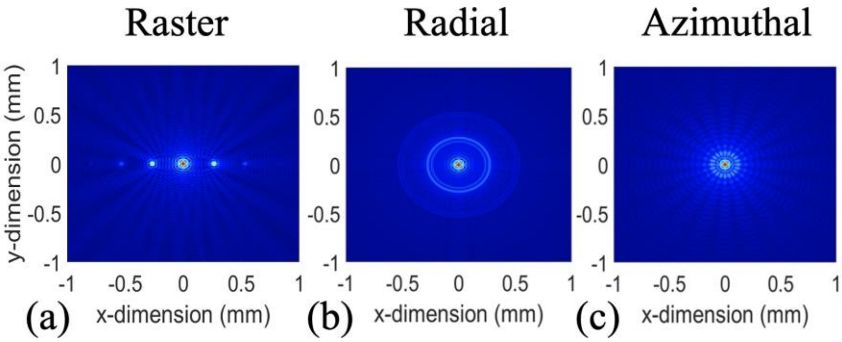

Figure 2-4: Qualitative comparison of aberrated PSFs for example cases discussed above after normalization to the diffraction-limited PSF and taking the 4th root to increase image contrast. [Reprinted] with permission from [10] © Optica Publishing Group.

The normalized absolute Fourier transform of the PSF is taken to obtain the aberrated MTF. We then use Eq. (2.1) (with the MTF) to obtain the relative modulation from the far field estimate. Next, we use Eq. (2.11) to estimate the relative modulation from the 2nd and 4th PDPD moments, as shown in Figure 2-5(a-c).

Finally, we take the difference between the relative modulation estimated from the 2nd and 4th PDPD moments and the relative modulation from the far-field calculation. As shown in Figure 2-5(d-f), the difference between the two approaches is <1% for most image space spatial frequencies. The exceptions are for relative modulation values that approach the cut-off frequencies; these more significant errors in the estimate are due to the decrease in the number of data points in the PDPD moments as the pupil shift reaches its maximum, where few data points exist. It should also be pointed out that there is a slight resolution difference between the estimated and far-field relative modulations. This leads to a small (~0.1%) asymmetry in the percentage difference. We note these results from the current examples with simple sinusoidal errors are obtained with only the 2nd and 4th moments, but the more general form of Eq. (2.10) with higher order moments may be needed for more complex MSF structures.

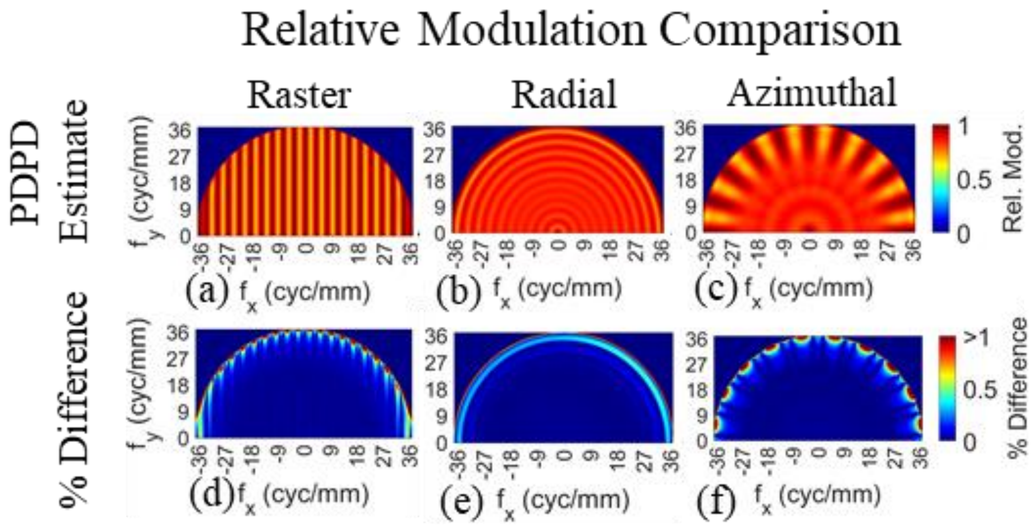

Figure 2-5: (a-c) Relative modulation from estimated from PDPD moments; (d-f) percentage difference maps between the two methods. Note, we transform the pupil shift to image space spatial frequency using Eq. (2.4) for both calculations. [Reprinted] with permission from [10] © Optica Publishing Group.

2.5 Discussion and Conclusion

In summary, we have reported on the derivation, development, and use of PDPD moments to specify generalized MSF errors for PDPD distributions without assumption of the distribution or stationarity of the PDPD. We demonstrated that the 2nd and 4th PDPD moments can be used to estimate the relative modulation to within 1% for simple MSF structures with symmetric PDPDs. Future work will explore the use of the PDPD moments to determine additional optics performance metrics and facilitate tolerancing of experimental MSF errors in optical imaging systems.

2.6 References

1. J. P. Rolland, M. A. Davies, T. J. Suleski, C. Evans, A. Bauer, J. C. Lambropoulos, and K. Falaggis, "Freeform optics for imaging, " Optica **8**, 161 (2021).
2. D. M. Aikens, J. E. DeGroote, and R. N. Youngworth, "Specification and Control of Mid-Spatial Frequency Wavefront Errors in Optical Systems, " in Frontiers in Optics 2008/Laser Science XXIV/Plasmonics and Metamaterials/Optical Fabrication and Testing, OSA Technical Digest (CD) paper OTuA1 (2008).
3. J. M. Tamkin and T. D. Milster, "Effects of structured mid-spatial frequency surface errors on image performance," Appl. Opt. **49**, 6522 (2010).
4. H. Aryan, G. D. Boreman, and T. J. Suleski, "Simple methods for estimating the performance and specification of optical components with anisotropic mid-spatial frequency surface errors, " Opt. Express **27**, 32709 (2019).
5. J. M. Elson and J. M. Bennett, "Calculation of the power spectral density from surface profile data, " Appl. Opt. **34**, 201 (1995).

6. R. E. Parks, O. P. Group, and N. C. Cima, "Specifications: Figure and Finish are not enough, " Proc. SPIE **7071**, 70710B (2008).

7. R. Zhelem, "Specification of optical surface accuracy using the structure function, " Proc. SPIE **8083**, 808310 (2011).

8. T. Pertermann, J. Hartung, M. Beier, M. Trost, S. Schröder, S. Risse, R. Eberhardt, A. Tünnermann, and H. Gross, "Angular resolved power spectral density analysis for improving mirror manufacturing, " Appl. Opt. **57**, 8692 (2018).

9. L. He, C. J. Evans, and A. Davies, "Two-quadrant area structure function analysis for optical surface characterization, " Opt. Express **20**, 23275 (2012).

10. Z. Hosseinimakarem, A. D. Davies, and C. J. Evans, "Zernike polynomials for mid-spatial frequency representation on optical surfaces, " Proc. SPIE **9961**, 99610P (2016).

11. G. W. Forbes, "Never-ending struggles with mid-spatial frequencies, " Proc. SPIE **9525**, 95251B (2015).

12. R. J. Noll, "Effect of Mid- and High-Spatial Frequencies on Optical Performance, " Opt. Eng. **18**, 182137 (1979).

13. J. E. Harvey and A. K. Thompson, "Scattering effects from residual optical fabrication errors, " Proc. SPIE **2576**, 155 (1995).

14. R. N. Youngworth and B. D. Stone, "Simple estimates for the effects of mid-spatial-frequency surface errors on image quality, " Appl. Opt. **39**, 2198 (2000).

15. K. Liang, G. W. Forbes, and M. A. Alonso, "Validity of the perturbation model for the propagation of MSF structures in 3D, " Opt. Express **28**, 20277 (2020).

16. K. Liang and M. A. Alonso, "Understanding the effects of groove structures on the MTF, " Opt. Express **25**, 18827 (2017).
17. K. Liang and M. A. Alonso, "Effects on the OTF of MSF structures with random variations, " Opt. Express **27**, 34665 (2019).
18. H. H. Hopkins, "The Aberration Permissible in Optical Systems, " Proc. Phys. Soc. B **70**, 449 (1957).
19. C. Olson, "Lens Performance Budgeting Using the Hopkins Ratio, " Opt. Photonics News 12 (2008).
20. L. Mandel and E. Wolf, *Optical Coherence and Quantum Optics*, (Cambridge University Press, 1995).
21. J. W. Goodman, *Introduction to Fourier Optics*, 4th ed. (W.H. Freeman, 2017).
22. Reference [16] states that the PDPD is symmetric in phase difference, but we do not believe that this is required. For example, a MSF distribution with a blazed profile would produce a non-symmetric PDPD. We identify the assumption here for clarity.
23. P. H. Westfall, “Kurtosis as Peakedness, 1905–2014. R.I.P.”, American Statistician **68**, 191 (2014).
24. G. D. Boreman, *Modulation Transfer Function in Optical and Electro-Optical Systems*, 2nd ed. (SPIE PRESS, 2021).

CHAPTER 3: ON THE USE OF PUPIL-DIFFERENCE MOMENTS FOR PREDICTING OPTICAL PERFORMANCE IMPACTS OF GENERALIZED MSF SURFACE ERRORS

3.1 Abstract

In this work, we present a methodology for predicting the optical performance impacts of random and structured MSF surface errors using pupil-difference probability distribution (PDPD) moments. In addition, we show that, for random MSF surface errors, performance estimates from the PDPD moments converge to performance estimates that assume random or Gaussian statistics. Finally, we apply these methods to several MSF surface errors with different distributions and compare how estimated optical performance values compare to predictions based on earlier methods assuming random error distributions.

3.2 Introduction

Sub-aperture manufacturing methods are key enablers for freeform optics [1]. However, one drawback to sub-aperture processes is the potential to introduce mid-spatial frequency (MSF) surface errors [2-6], which can take considerable effort to mitigate [7-16]. MSF surface errors fall between ‘low-frequency’ form errors and ‘high-frequency’ roughness errors, with ambiguous lower and upper bounds [17]. Understanding the impacts of MSF errors on optical performance is important to the larger optics community as such errors can cause small angle scatter [18-19], degrade image performance [20-23], and result in self-imaging [24,25] and distortion [26,27].

MSF surface errors are commonly observed with a broad range of structured distributions (e.g., raster, radial, azimuthal) that are related to the manufacturing method

[17,28]. Previous methods for predicting the performance impacts of MSF surface errors on image quality have relied on assumptions of random or Gaussian error distributions [18,29,30]. A common approach is to estimate the Strehl ratio from the surface RMS error [30]. This approach will provide a baseline performance estimation for random surfaces in this work. However, different MSF distributions with similar simple surface metrics (i.e., root mean square (RMS) surface error (σ), slope, Peak-Valley (PV)) can have drastically different optical performance [1,31,32]. Therefore, specification methods that connect general MSF surface errors to optical performance are desirable.

To this end, additional metrics such as the minimum modulation curve (MMC) [33] and Q' [31] have been recently proposed. The MMC metric quantifies the lowest values in the 2D modulation transfer function (MTF) as a function of radial image space spatial frequency and azimuthal angle, while Q' quantifies the normalized area under the MMC and is analogous to the Strehl ratio. These methods are inspired by the 1D modulation transfer function (MTF) and its relationship to the Strehl ratio [34], but better quantify and distinguish between the optical performance impacts of deterministic MSF surface errors and also agree with predictions from earlier statistical methods [30] for cases with uniform or random MSF surface errors [31]. However, we note that previous connections of the MMC and Q' to surface specifications were largely empirical [31]. Pupil-Difference Probability Distributions (PDPD) were recently introduced by Alonso and Liang as a tool to show the impact of MSF groove structures and their random variations on the optical transfer function (OTF) [35,36]. Building on that work, we have recently shown that the PDPD moments have desirable properties for specification of general MSF surface errors and for connecting those specifications to relative optical modulation [32].

In this paper, we build on the work from [32] to demonstrate use of the PDPD moments to connect both random and structured MSF error distributions to the MMC, Strehl ratio, and Q'. We first summarize the measures of optical performance used in this work. We then investigate the relationship of the 2nd PDPD moments to σ to quantitatively explore the convergence of predicted optical performance from random and deterministic MSF error distributions. For cases that do not converge, we then provide a procedure relating the 2nd and 4th PDPD moments to the minimum modulation curve [33] and Q' [31]. Finally, we demonstrate the application of these methods to several examples with different MSF distributions and levels of randomness and compare how estimated optical performance values compare to predictions based on earlier methods assuming random error distributions.

3.3 Measures of Optical Performance for MSF Errors

3.3.1 Strehl Ratio

The Strehl Ratio *S* quantifies the ratio of the peak value of the point spread function (PSF) of an aberrated optical system to the peak value for an ideal diffraction-limited system [34]. While there are multiple methods to calculate the Strehl Ratio [37-43], we use two forms in this work. The first definition is calculated from the area under the aberrated (‘AB’) MTF normalized by the area under the diffraction-limited (‘DL') MTF [34], as shown in Eq. (3.1):

$$S = \frac{\iint MTF_{AB}(f_x, f_y) df_x df_y}{\iint MTF_{DL}(f_x, f_y) df_x df_y} \tag{3.1}$$

The second definition is an exponentially decaying approximation proposed for use with MSF errors by Youngworth and Stone [30], as shown in Eq. (3.2):

$$S \approx \exp[-k^2(\Delta n)^2\sigma^2] \tag{3.2}$$

where Δn is the index contrast and k is the wavenumber. With either definition of the Strehl ratio, the aberrated MTF can be estimated by multiplying S by the diffraction-limited MTF, as shown in Eq. (3.3).

$$MTF_{AB}(f_x, f_y) \approx (S)MTF_{DL}(f_x, f_y) \tag{3.3}$$

One challenge with the Strehl ratio is that it can result in misleading predictions of optical performance with deterministic MSF errors. To illustrate this point, we calculate the Strehl ratio for both a Gaussian error distribution, Figure 3-1(a), and for a structured raster MSF signature, Figure 3-1(b). The Gaussian surface has a PV = 598 nm and an σ = 70 nm. The structured raster MSF signature used in this example has a period of 0.2 mm, PV = 200 nm, and σ = 70 nm. Note that we scaled the Gaussian surface to have nearly the same σ and did not control the PV. In order to achieve a specific PV for the Gaussian surface, the relative phase angles of the spectra would need to be controlled [44,45]. However, for the following examples, having an equivalent σ is sufficient. Both surfaces are superimposed onto separate but identical plano-convex lenses at the aperture stop with 100 mm focal length, diameter D = 2 mm, and Δn = 0.49 at a source wavelength of 532 nm, as shown in Figure 3-1(c).

For both cases, we then calculate the PSF from the absolute magnitude squared of the propagated field via a Fourier Transform to the image plane under far-field assumptions, and then calculate the 2D MTF by taking the magnitude of the Fourier transform of the PSF. A cross-section of the 2D MTF along the x-axis for the lens with Gaussian surface is shown in Figure 3-1(d) and for the lens with the structured MSF in Figure 3-1(e). In addition, the MTF is estimated from Eq. (3.3), with $S = 0.84$ from both Eqs. (3.1) and (3.2) in each case. From Figure 3-1(d), we see that random errors are well estimated by the Strehl ratio but Figure 3-1(e) shows that the Strehl ratio underestimates the impacts of the deterministic MSF error on MTF.

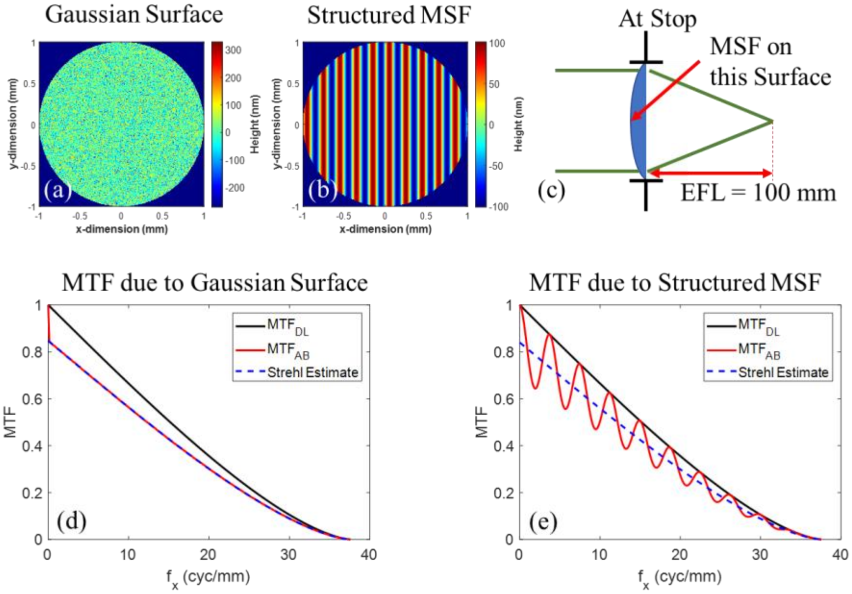

Figure 3-1: (a) Gaussian surface error; (b) structured raster MSF error, (c) optical system used in example; (d) MTF and Strehl estimate for Gaussian surface case; (e) MTF and Strehl estimate for Structured MSF case.

3.3.2 MMC and Q′

As discussed in Section 3.2, the minimum modulation curve (MMC) [33] and Q' [31] were recently proposed to better estimate optical performance impacts of more general MSF errors. The MMC is a useful metric because it accounts for the directionality that MSF errors may have but also reduces to estimates given by Strehl ratio for random surface error distributions [31]. Analogous to the Strehl ratio, Q' is quantified by calculating the area under the MMC normalized by the area under the diffraction-limited MTF [31], as shown in Eq. (3.4). The MMC can be estimated from Q' using Eq. (3.5).

$$Q' = \frac{\int MMC(\rho)d\rho}{\int MTF_{DL}(\rho)d\rho} . \tag{3.4}$$

$$MMC(\rho) \approx (Q')MTF_{DL}(\rho) . \tag{3.5}$$

In Figure 3-2 below, we calculate the MMC and Q' from the MSF example in Figure 3-1. Using Eq. (3.4), we calculate $Q' = 0.69$ and then use Eq. (3.5) to estimate the MMC. We see that Q' better estimates the performance impacts of the MSF error on this lens because it captures the oscillations in the MTF.

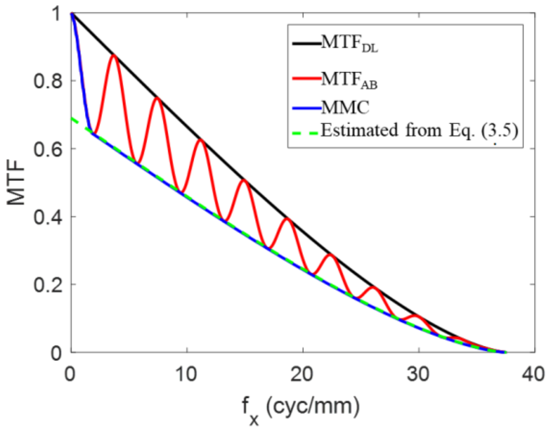

Figure 3-2: MMC and Q' predictions of optical performance impacts of MSF errors from Figure 3-1.

3.4 Convergence of Performance Estimates Between Random and Deterministic MSF Error Distributions

The examples in Section 3.3.1 illustrate differences in optical performance predictions for random and deterministic MSF error distributions. We now consider use of the relative optical modulation M to investigate the convergence of performance estimates between random and deterministic cases. As described in [32], M is a multiplicative factor to the MTF that captures information on the MSF error distribution. Under the assumptions of a symmetric PDPD, small drops in relative modulation, and an MSF error surface at the exit pupil, the 2nd and 4th PDPD moments can be used to estimate the relative modulation as shown in Eq. (3.6):

$$M(\tau_x,\tau_y) \approx 1 - k^2(\Delta n)^2 \frac{\left\langle H_C^2(\tau_x,\tau_y)\right\rangle}{2!} + k^4(\Delta n)^4 \frac{\left\langle H_C^4(\tau_x,\tau_y)\right\rangle}{4!} \,. \tag{3.6}$$

In Eq. (3.6) the pupil shift vector τ_i is a generalization of image space spatial frequency and is used to describe the location of the PDPD moment value in the PDPD moment map [32]. For PDPD moment maps shown in this work, τ_x ranges from $-D$ to D, and τ_y ranges from 0 to D. Note that the negative axis is not shown for τ_y to avoid redundancy in the PDPD moment maps [32,46].

We now use Eq. (3.6) to compare performance estimates between surfaces with random and structured MSF error distributions. We start by assuming the PDPD has a zero-mean pupil-difference for all pupil shifts, as was done for the area structure function [46]. We then expand out the 2nd PDPD moment terms, as shown in Eq. (3.7):

$$\left\langle H_c^2(\tau_x,\tau_y)\right\rangle = \left\langle h^2(x,y)\right\rangle + \left\langle h^2(x-\tau_x,y-\tau_y)\right\rangle - 2\left\langle h(x,y)h(x-\tau_x,y-\tau_y)\right\rangle \,. \tag{3.7}$$

When the height distribution $h(x,y)$ is stationary [46,47], the first and second terms are equivalent and the 2nd PDPD moment can be approximated as:

$$\left\langle H_c^2(\tau_x,\tau_y)\right\rangle \approx 2\left\langle h^2(x,y)\right\rangle - 2\left\langle h(x,y)h(x-\tau_x,y-\tau_y)\right\rangle = 2\sigma^2 - 2\left\langle h(x,y)h(x-\tau_x,y-\tau_y)\right\rangle \,. \tag{3.8}$$

This shows that the 2nd PDPD moment is proportional to σ^2 and an autocovariance term. The autocovariance term can oscillate from $-\sigma^2$ (perfectly anti-correlated) to $+\sigma^2$ (perfectly correlated) and will tend towards zero at small pupil-shifts for random surfaces [29].

To further illustrate this point, we calculate the 2nd PDPD moments for the raster sinusoidal MSF error and random Gaussian surface used in Section 3.3.1. The 2nd PDPD moments of the Gaussian and structured MSF are calculated using the procedure defined in [32] and are shown in Figures 3-3(a) and 3-3(b), respectively. We then take the cross-sections of the 2nd PDPD moments along the $+\tau_x$ direction from zero to D at $\tau_y = 0$ for both cases, as shown in Figures 3-3(c) and 3-3(d). From Figure: 3-3(c), we see that the 2nd PDPD moment of the Gaussian surface lies close to the mean of $2\sigma^2$. From Figure 3-3(d), we see that the 2nd PDPD moment oscillates around the mean of $2\sigma^2$ and peaks at twice the mean due to the deterministic structure of the raster MSF error. This description holds well until we reach the edges of the 2nd PDPD moment due to a decreasing number of data points in the PDPD. It is clear that the 2nd PDPD moment amplitude for random surface errors with little correlation will lie close to $2\sigma^2$, and for structured raster MSF the 2nd PDPD moment amplitude will oscillate around the mean of $2\sigma^2$ up to a maximum of twice the mean.

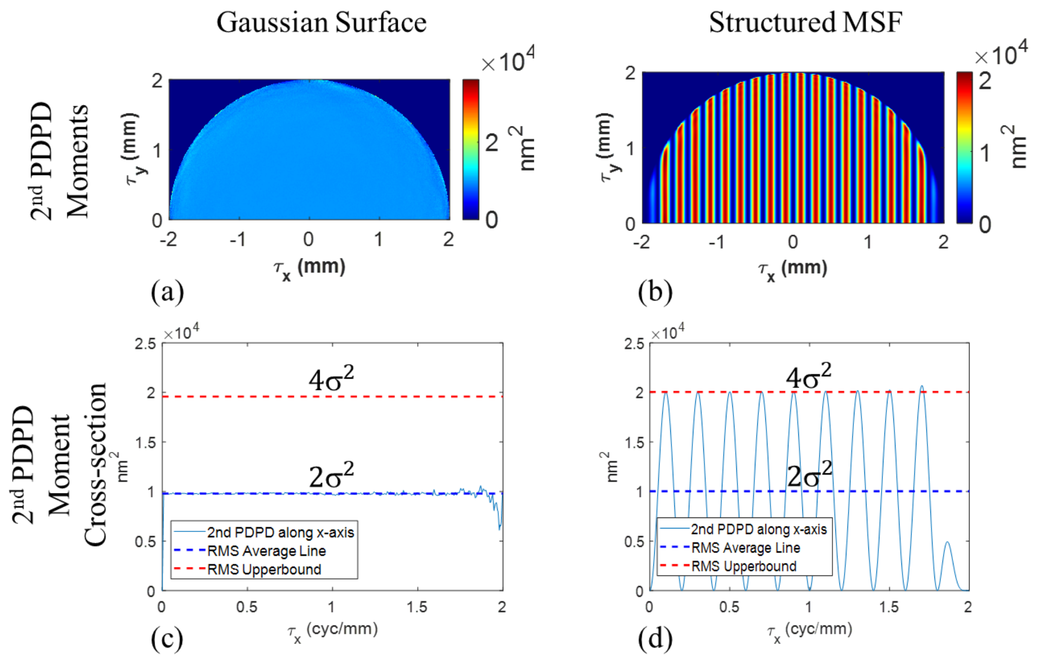

Figure 3-3: (a) 2nd PDPD moment of Gaussian surface error, (b) 2nd PDPD moment of Structured MSF, (c) cross-section along the $+\tau_x$, direction from zero to D at $\tau_y = 0$ of 2nd PDPD moment from Gaussian surface, and (d) cross-section of 2nd PDPD moment along $+\tau_x$, from zero to D at $\tau_y = 0$ from the structured MSF example.

To see how Eq. (3.6) relates to the Strehl ratio associated with random surfaces, we consider only up to the second term of Eq. (3.6) and substitute $2\sigma^2$ in the second term, which is the 2nd PDPD moment result for random surfaces. In this case, the estimated relative modulation, shown in Eq. (3.9), is approximately equal to the first two terms in a Taylor series expansion of the Strehl ratio from Eq. (3.2), which is valid under a weak aberration scenario [37].

$$M_{uncorrelated}(f_x, f_y) \approx 1 - k^2(\Delta n)^2\sigma^2 \approx S \ . \tag{3.9}$$

If the same k, Δn, and system from Section 3.3.1 are used with Eq. (3.9), then $M_{uncorrelated} \approx 0.84$, which is the same result that was reached using Eqs. (3.1) and (3.2).

This implies that the Strehl ratio is a good measure of optical performance impact when surface errors are random. This result is supported by previous works that assume Gaussian statistics of surface errors to estimate the impact on the transfer function [18,29]. However, we note here that (unlike previous works) the use of the PDPD moments makes no assumption of Gaussian statistics to relate the surface specification to optical performance.

Applying a similar process for the structured MSF case, we have an upper bound estimate of the 2nd PDPD moments impact on the relative modulation, shown in Eq. (3.10). Once again, using the same k and Δn, we estimate $M_{correlated} \approx 0.67$ which is closer to the Q' estimate in Section 3.3.2.

$$M_{correlated}(f_x, f_y) \approx 1 - 2k^2(\Delta n)^2\sigma^2 \approx Q' . \tag{3.10}$$

Note that the slight deviation between the Q' from Section 3.3.2 and $M_{correlated}$ is attributed to the truncation of the series used to derive Eq. (3.10). We see clearly from this analysis that Strehl ratio can be a poor estimate of optical performance for structured MSF errors and that the use of PDPD moments can facilitate better performance predictions in such cases.

Up to this point, we have only shown how the 2nd PDPD moment relates to σ and how the relative modulation (up to the 2nd term) converges to the Strehl ratio under a random surface assumption. A logical next step would be to consider a similar process including the 4th PDPD moment. To do so we would need to assume that Gaussian moment theorem [47] could be applied to the higher-order terms in the 4th PDPD moment expansion. However, we emphasize that MSF error distributions may not be Gaussian. Rather than making assumptions on the surface statistics, we propose a procedure that utilizes the generality of the PDPD moments to predict the impacts of MSF errors on optical performance regardless of their correlation.

3.5 Optical Performance Predictions from PDPD Moments

3.5.1 Standard Error in PDPD Moments

Before estimating the optical performance using the PDPD moments, the influence on regions in the PDPD moment maps with few data points must be considered. Figure 3-4 shows that the number of data points changes from many to few as the pupil shift varies in the PDPD calculation, and each instance of the PDPD has a finite amount of data points from which to calculate the moments, as shown in Figure 3-4(c).

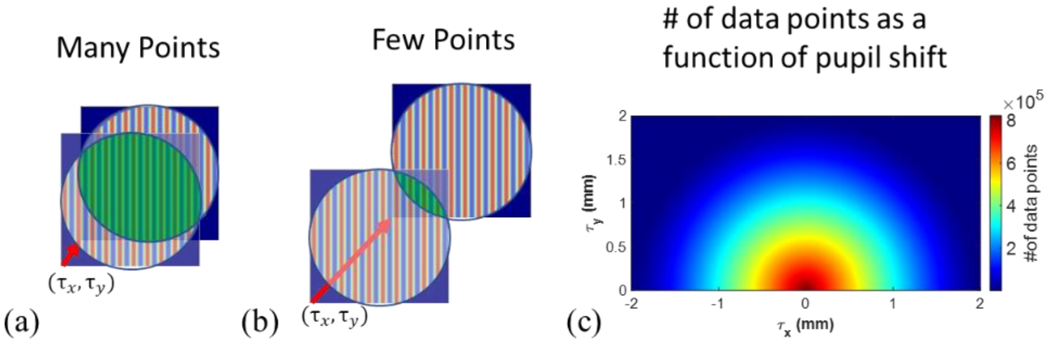

Figure 3-4: (a) PDPD using many points, (b) PDPD using few points, (c) map of number of data points used in each PDPD pupil shift instance.

To assess the amount of error due to the discreteness of calculating PDPD moment data, we propose use of the *standard error* [48]. The standard error can be thought of as the variance in calculating a moment from a limited data set. Not all moments have easy-to-express relationships to standard error. However, the 2nd moment has a tractable form and does not make statistical assumptions in its formulation. As defined by Rao, the standard error of the 2nd moment (the variance) is shown in Eq. (3.11) [48] where m is the number of points in the distribution, σ^2 is the variance, and κ is the 4th moment. We must rewrite Eq. (3.11) as a function of pupil shift to apply this method to the 2nd PDPD moments. The standard error of the 2nd PDPD moment is shown in Eq. (3.12). The normalized standard error (NSE) can then be calculated by dividing through by the 2nd PDPD moments, as shown in Eq. (3.13). Note that the NSE is undefined for a 2nd PDPD moment of zero value (which occurs at zero pupil-shift).

$$SE[\sigma^2] = \sqrt{\frac{(m-1)^2}{m^3}\left(\kappa + \frac{(m-3)}{(m-1)}\sigma^4\right)} \tag{3.11}$$

$$SE[\langle H_C^2(\tau_x,\tau_y)\rangle] = \sqrt{\frac{(m(\tau_x,\tau_y)-1)^2}{m(\tau_x,\tau_y)^3}\left(\langle H_C^4(\tau_x,\tau_y)\rangle + \frac{(m(\tau_x,\tau_y)-3)}{(m(\tau_x,\tau_y)-1)}\langle H_C^2(\tau_x,\tau_y)\rangle^2\right)} \tag{3.12}$$

$$NSE = \frac{SE[\left\langle H_C^2(\tau_x,\tau_y)\right\rangle]}{\left\langle H_C^2(\tau_x,\tau_y)\right\rangle}. \tag{3.13}$$

A similar process can be performed for the 4th PDPD moment, but the expression is less tractable. The standard errors for specific 4th moment values can be calculated by bootstrapping or jackknifing approaches [49], but this is outside the scope of the present work.

With the normalized standard error map, a particular threshold can be applied (for example, 1%), and then a mask of all the 2nd PDPD moments with a normalized standard error less than 1% can be multiplied by the 2nd PDPD moment map to exclude those values from assessment, as shown in Figures 3-5 and 3-6, respectively. The same mask should also be applied to the 4th PDPD moment map since those pupil shift locations won't be considered in the 2nd PDPD moment map.

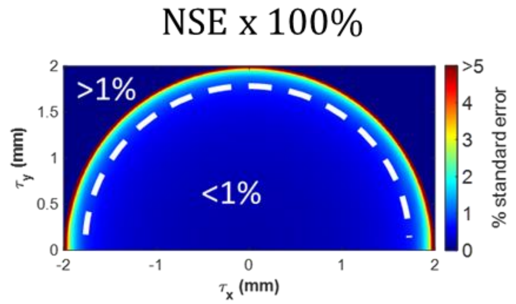

Figure 3-5: Normalized standard error map for structured MSF example from Figure 3-1(b) with a 1% threshold.

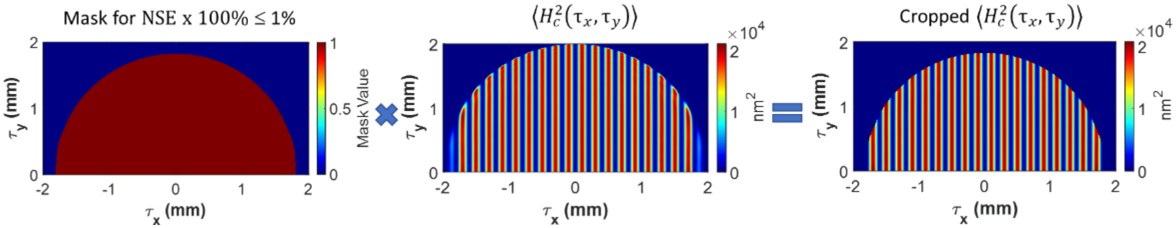

Figure 3-6: Example masking out points in the 2nd PDPD moment with normalized standard errors greater than 1%.

3.5.2 PDPD moments relationship with Q′ and estimating the MMC

To connect the PDPD moments to Q', we start at Eq. (3.6). We note that Eq. (3.6) captures the full range of relative modulation. From the form of Eq. (3.6) it is clear that the minimum relative modulation will be found for the condition in which the 2nd PDPD moment is a maximum. The 4th PDPD maxima also follows this trend. As a result, we assert that Q' can be estimated by using the PDPD moment maxima in Eq. (3.6) to obtain:

$$Q' \approx 1-\frac{k^2(\Delta n)^2\left\langle H_c^2(\tau_x,\tau_y)\right\rangle_{\max}}{2!}+\frac{k^4(\Delta n)^4\left\langle H_c^4(\tau_x,\tau_y)\right\rangle_{\max}}{4!}\,. \qquad (3.14)$$

The MMC can then be estimated from Eq. (3.5). It should be noted that the maxima in the 2nd and 4th PDPD moments may not always occur at the same pupil shift values, in which case Eq. (3.14) may lose some accuracy. In this case, we suggest looking for the relative modulation's lowest value, estimated from Eq. (3.6), and then reporting 2nd and 4th PDPD moment values at that particular pupil shift to better estimate the MMC. To account for this point and the standard error of the PDPD moments, we propose the following process:

1) Calculate the 2nd and 4th PDPD moments from the MSF surface error.

2) Calculate the standard error of the 2nd PDPD moments.

3) Apply a chosen threshold to the normalized standard error and crop out 2nd and 4th PDPD moments for all pupil shift values above that threshold.

4) Apply Eq. (3.6) to estimate the relative modulation.

5) Find the lowest relative modulation from Eq. (3.6) and calculate the 2nd and 4th PDPD moments for those pupil shift values.

6) Estimate Q' using Eq. (3.14).

7) Apply Eq. (3.5) to estimate the MMC.

We use the MSF example from Section 3.2.1 with the same *Δn* and *k* values as before to illustrate the workflow, as shown in Figure 3-7. The estimate of $Q' \approx 0.68$ is within 1% of the estimate from Eq. (3.4).

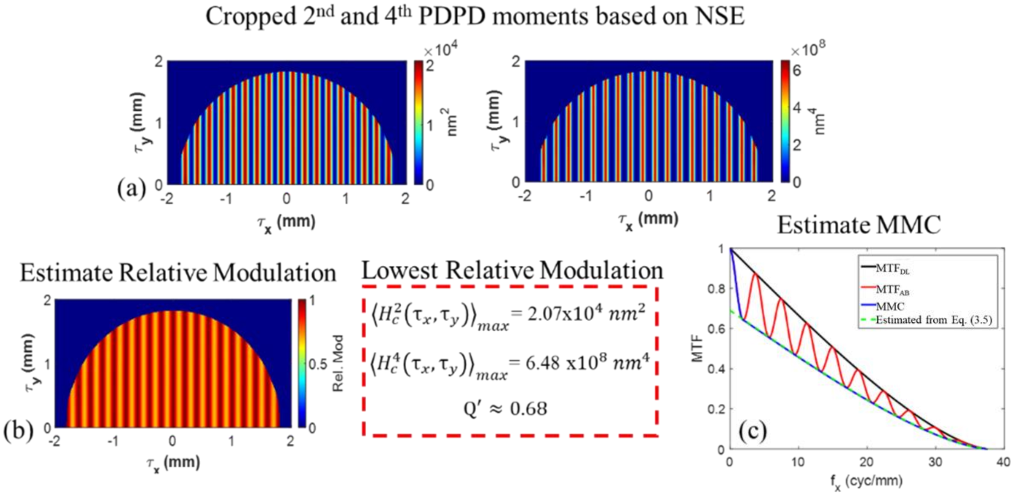

Figure 3-7: Workflow for example MSF surface from Section 3.3.1 (a) cropped 2nd and 4th PDPD moments, (b) estimate of Q' from PDPD moments maxima, (c) estimated MMC using Eq. (3.5).

3.6 Examples: Estimating Optical Performance of Different MSF Distributions

We now compare specification and performance predictions for several different MSF surface error distributions (Figure 3-8) using the general procedures outlined in Section 3.5.2 and the procedures for random surface errors.

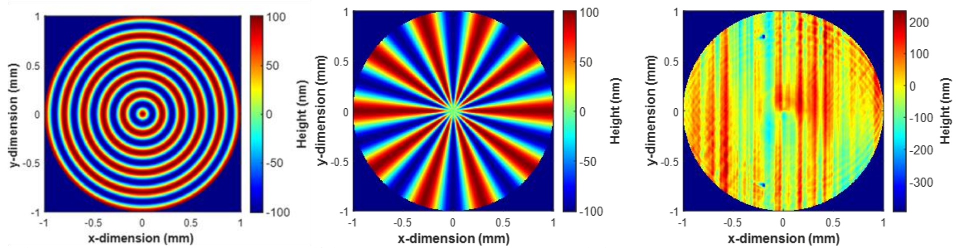

(a) (b) (c)

Figure 3-8: (a) Radial sinusoidal MSF; (b) Azimuthal sinusoidal MSF; (c) Experimental raster MSF.

We also include the results from the earlier raster and Gaussian surfaces in this analysis for additional comparison. The σ for all examples differ slightly due to their periodicity and distribution but are all ~70 nm.

To compare the procedure in Section 3.5.2 to the procedures for random surfaces, we do the following: (1) Tabulate the maxima of the 2nd and 4th PDPD moments following Section 3.5.2; (2) Calculate $2\sigma^2$ for each surface. These values are included to show that performance estimates from Section 3.5.2 and random surface methods converge when the 2nd PDPD moment peak value is close to $2\sigma^2$; (3) Calculate Q' values from the MMC (Eq. (3.4)) and PDPD moments (Eq. (3.14)); and (4) Calculate the Strehl ratio from the MTF (Eq. (3.1)) and from σ (Eq. (3.2)), all using the same Δn and k values from Section 3.3.1. A summary of these results is shown in Table 3-1.

Table 3-1: Surface statistics and optical performance metrics for example MSF surfaces

Surface	**2nd PDPD$_{max}$ (nm^2)**	**$2\sigma^2$ (nm^2)**	**4th PDPD$_{max}$ (nm^4)**	**Strehl (Eq. (3.1))**	**Strehl$_\sigma$ (Eq. (3.2))**	**Q' (Eq. (3.4))**	**Q'_{PDPD} (Eq. (3.14))**
Raster	2.07x10^4	1.01x10^4	6.48x10^8	0.84	0.84	0.69	0.68
Radial	1.40x10^4	1.01x10^4	3.64x10^8	0.84	0.84	0.84	0.78
Azimuthal	1.99x10^4	1.00x10^4	5.87x10^8	0.84	0.85	0.84	0.69
Experimental	1.51x10^4	1.00x10^4	7.15x10^8	0.85	0.85	0.82	0.78
Gaussian	1.07x10^4	1.00x10^4	3.58x10^8	0.85	0.85	0.84	0.84

From Table 3-1, we note that cases with a 2nd PDPD maximum close to $2\sigma^2$ tend to be appropriately specified by σ, and its performance will be closely estimated by the Strehl ratio. The 2nd PDPD maximum of the example Gaussian surface is closest to $2\sigma^2$, and we observe that performance in this case is well predicted by the Strehl ratio. A general trend can be observed that larger deviations between the 2nd PDPD maxima and $2\sigma^2$, correspond to larger deviations between the Strehl ratio performance estimates and Q'. Results are also shown in Figure 3-9 for each case through plots of the diffraction-limited performance, the MTF estimated from Eq. (3.3), the MMC, and the MMC estimated by Eq. (3.5).

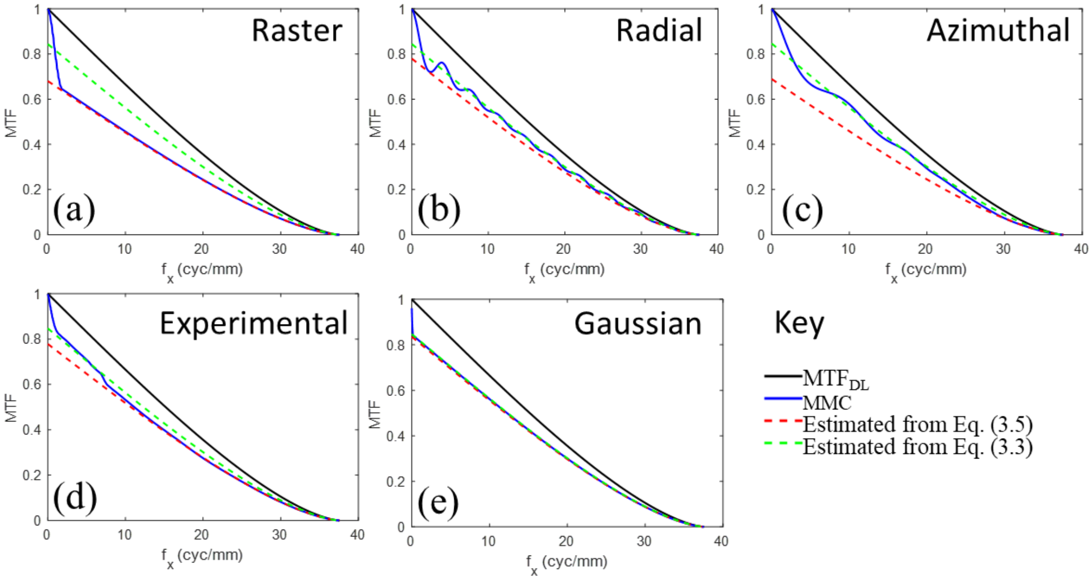

Figure 3-9: MMC comparisons with diffraction-limited case and Strehl estimate of MTF for (a) Raster MSF surface example, (b) Radial MSF surface example, (c) Azimuthal MSF surface example, (d) Experimental MSF surface example, and (e) Gaussian surface example.

An additional observation from Table 3-1 is that the MMC calculation of Q' does not always closely match the Q' estimate from Section 3.5.2. This is because the PDPD moment maxima are calculated from the lowest relative modulation value, while the MMC calculation of Q' comes from the average of the lowest 2D MTF values. This nuance is best visualized in Figures 3-9(b) and 3-9(c), where we see the MMC estimated by Section 3.5.2 methods only touches one point on the MMC, at the point of lowest relative optical modulation.

3.7 Summary and Discussion

We have demonstrated a procedure using the PDPD moments of MSF surface errors to predict reductions in optical performance and shown that the 2nd and 4th PDPD moments can be utilized to estimate the optical performance impacts of both random and deterministic MSF surface errors. For random surfaces, the estimates using PDPD moments converge to estimates using the Strehl ratio with random surface errors. We showed that optical performance is well predicted using methods based on the Strehl ratio for surfaces for which the 2nd PDPD moment maximum is close to the mean. However, we also saw a large variation in optical performance predictions for the range of MSF surface error distributions presented. As a result, we saw it valuable and necessary to utilize the 2nd and 4th PDPD moment procedures for most cases. Use of PDPD moments as proposed herein enables improved predictions of the impacts of generalized MSF errors on optical performance in imaging systems at the cost of increased calculation complexity. Ultimately a decision must be made on how precisely the optical performance must be predicted to determine if it is necessary to utilize the PDPD moments.

We note a limitation in that the moment maps can have large standard errors when used with low-resolution height maps. It is recommended to use surface height maps that are nominally of the size of (at least) 1000 x 1000 pixels if possible. Using smaller height maps may not properly resolve the MSF errors and may also produce large errors in optical performance predictions. A separate challenge is that the PDPD moment maps can be challenging to interpret due to the multi-dimensional nature of the statistics. We utilize the maxima of the moment maps in the current work, but note that additional information regarding the surface errors is also contained, such as period [46] and slope [50].

With the above limitations in mind, we provide this work to help readers gauge if a given MSF error distribution can be adequately specified using σ or if the additional information provided by the PDPD moments is needed for their specific case. We also note that the maxima of the PDPD moments provide single-value metrics that can be reported with little interpretation of the moment maps as a whole. This result suggests that the calculation of the maxima could be automated, and the values used as straightforward pass/fail criteria for specification and acceptance testing.

Lastly, we note opportunities for future expansion of this work. As discussed in [32], in cases where the 3rd PDPD moment is non-zero, the complex component of the relative modulation will also be non-zero, and the estimate from Section 3.5.2 may not be valid. We plan to extend this work to include the analysis of the 3rd PDPD moment and provide additional procedures that consider a complex component to the relative modulation. In addition, we note that the aberrated 2D MTF can be estimated by multiplying Eq. (3.6) by the 2D diffraction-limited MTF. This approach could help to facilitate defining optical performance over specific band limits in image space and enable quantifying the impacts of MSF surface errors at targeted image space spatial frequencies.

3.8 References

1. J. P. Rolland, M. A. Davies, T. J. Suleski, C. Evans, A. Bauer, J. C. Lambropoulos, and K. Falaggis, "Freeform optics for imaging," Optica **8**, 161–176 (2021).
2. A. Sohn, L. Lamonds, and K. Garrard, "MODELING OF VIBRATION IN SINGLE-POINT DIAMOND TURNING," in Proc. ASPE 21st Annual Meeting (2006), pp. 15-20.
3. S. Rakuff and P. Beaudet, "Thermally induced errors in diamond turning of optical structured surfaces," Opt. Eng. **46**, 103401 (2007).

4. M. Pohl and R. Borret, "Simulation of mid-spatials from the grinding process," Eur. Opt. Soc.-Rapid **11,** 16010 (2016).
5. B. Zhong, H. Huang, X. Chen, W. Deng, and J. Wang, "Modelling and simulation of mid-spatial-frequency error generation in CCOS," J. Eur. Opt. Soc.-Rapid Publ. **14**, 4 (2018).
6. S. Wan, C. Wei, Z. Hong, and J. Shao, "Modeling and analysis of the mid-spatial-frequency error characteristics and generation mechanism in sub-aperture optical polishing," Opt. Express **28**, 8959–8973 (2020).
7. D. D. Walker and C. Dunn, "Pseudo-random tool paths for CNC sub-aperture polishing and other applications," Opt. Express **16**, 18942–18949 (2008).
8. D. Nelson, J. D. Nelson, A. Gould, C. Klinger, and M. Mandina, "Incorporating VIVE into the precision optics manufacturing process," Proc. SPIE **81261**, 812613 (2011).
9. T. Wang, H. Cheng, W. Zhang, H. Yang, and W. Wu, "Restraint of path effect on optical surface in magnetorheological jet polishing," Appl. Opt. **55**, 935–942 (2016).
10. H. Shahinian, M. Hassan, H. Cherukuri, and B. A. Mullany, "Fiber-based tools: material removal and mid-spatial frequency error reduction," Appl. Opt. **56**, 8266–8274 (2017).
11. A. Beaucamp, K. Takizawa, Y. Han, and W. Zhu, "Reduction of mid-spatial frequency errors on aspheric and freeform optics by circular-random path polishing," Opt. Express **29**, 29802–29812 (2021).
12. S.-W. Liu, H.-X. Wang, Q.-H. Zhang, J. Hou, X.-H. Chen, Q. Xu, and C. Wang, "Smoothing process of conformal vibration polishing for mid-spatial frequency

errors: characteristics research and guiding prediction," Appl. Opt. **60**, 3925–3935 (2021).

13. K. Wan, S. Wan, C. Jiang, C. Wei, and J. Shao, "Sparse bi-step raster path for suppressing the mid-spatial-frequency error by fluid jet polishing," Opt. Express **30**, 6603–6616 (2022).
14. C. Wang, Y. Han, H. Zhang, C. Liu, L. Jiang, and L. Qian, "Suppression of mid-spatial-frequency waviness by a universal random tree-shaped path in robotic bonnet polishing," Opt. Express **30**, 29216–29233 (2022).
15. G. Chen and J. Qiao, "Femtosecond-laser-enabled simultaneous figuring and finishing of glass with a subnanometer optical surface," Opt. Lett. **47**, 3860–3863 (2022).
16. J. Coniglio, J. Beck, J. Odle, S. Murty, D. R. Brooks, and J. DeGroote Nelson, "Force controlled mid-spatial frequency error smoothing using machine learning," Proc. SPIE **12188** (2022), p. 121880P.
17. D. M. Aikens, J. E. DeGroote, and R. N. Youngworth, "Specification and control of mid-spatial frequency wavefront errors in optical systems," in Frontiers in Optics 2008/Laser Science XXIV/Plasmonics and Metamaterials/Optical Fabrication and Testing, OSA Technical Digest (CD) (Optical Society of America, 2008), paper OTuA1.
18. J. E. Harvey and A. K. Thompson, "Scattering effects from residual optical fabrication errors," Proc. SPIE **2576**, 155–174 (1995).

19. X. Lu and H. Gross, "Wigner function-based modeling and propagation of partially coherent light in optical systems with scattering surfaces," Opt. Express **29**, 14985–15000 (2021).
20. J. P. Marioge and S. Slansky, "Effect of figure and waviness on image quality," J. Opt. **14**, 189–198 (1983).
21. J. M. Tamkin, W. J. Dallas, and T. D. Milster, "Theory of point-spread function artifacts due to structured mid-spatial frequency surface errors," Appl. Opt. **49**, 4814–4824 (2010).
22. J. M. Tamkin, T. D. Milster, and W. Dallas, "Theory of modulation transfer function artifacts due to mid-spatial-frequency errors and its application to optical tolerancing," Appl. Opt. **49**, 4825–4835 (2010).
23. J. M. Tamkin and T. D. Milster, "Effects of structured mid-spatial frequency surface errors on image performance," Appl. Opt. **49**, 6522–6536 (2010).
24. V. P. Sivokon and M. D. Thorpe, "Theory of bokeh image structure in camera lenses with an aspheric surface," Opt. Eng. **53**, 065103 (2014).
25. K. Liang, G. W. Forbes, and M. A. Alonso, "Validity of the perturbation model for the propagation of MSF structures in 3D," Opt. Express **28**, 20277–20295 (2020).
26. G. Erdei, G. Szarvas, and E. Lorincz, "Tolerancing surface accuracy of aspheric lenses used for imaging purposes," Proc. SPIE **5249** (2004).
27. K. Achilles, K. Uhlendorf, and D. Ochse, "Tolerancing the impact of mid-spatial frequency surface errors of lenses on distortion and image homogeneity," Proc. SPIE **9626,** 96260A (2015).

28. L. A. DeMars, S. Rueda, and T. J. Suleski, "MSFLib: A Data Library of Mid-Spatial Frequency Surface Errors for Optical Modeling and Specification," in Optica Design and Fabrication (OFT), Paper OW4B.2 (2023).
29. R. J. Noll, "Effect of Mid- and High-Spatial Frequencies on Optical Performance," Opt. Eng. **18**, 137–142 (1979).
30. R. N. Youngworth and B. D. Stone, "Simple estimates for the effects of mid-spatial-frequency surface errors on image quality," Appl. Opt. **39**, 2198–2209 (2000).
31. H. Aryan, G. D. Boreman, and T. J. Suleski, "Simple methods for estimating the performance and specification of optical components with anisotropic mid-spatial frequency surface errors," Opt. Express **27**, 32709–32721 (2019).
32. L. A. DeMars and T. J. Suleski, "Pupil-difference moments for estimating relative modulation from general mid-spatial frequency surface errors," Opt. Lett. **48**, 2492–2495 (2023).
33. H. Aryan, G. D. Boreman, and T. J. Suleski, "The Minimum Modulation Curve as a tool for specifying optical performance: application to surfaces with mid-spatial frequency errors," Opt. Express **27**, 25551–25559 (2019).
34. G. D. Boreman, *Modulation Transfer Function in Optical and Electro-Optical Systems*, 2nd ed. (SPIE PRESS, 2021).
35. K. Liang and M. A. Alonso, "Understanding the effects of groove structures on the MTF," Opt. Express **25**, 18827–18841 (2017).
36. K. Liang and M. A. Alonso, "Effects on the OTF of MSF structures with random variations," Opt. Express **27**, 34665 (2019).

37. V. N. Mahajan, "Strehl Ratio for Primary Aberrations in Terms of Their Aberration Variance.," J. Opti. Soc. of Am. **73**, 860–861 (1983).
38. J. Ojeda-Castaneda, E. Andres, and P. Montes, "Phase-space representation of the Strehl ratio: ambiguity function," J. Opt. Soc. Am. A **4**, 313-317 (1987).
39. A. van den Bos, "Aberration and the Strehl ratio," J. Opt. Soc. Am. A **17**, 356-358 (2000).
40. C. J. R. Sheppard, "Maréchal condition and the effect of aberrations on Strehl intensity," Opt. Lett. **39**, 2354–2357 (2014).
41. M. A. Alonso and G. W. Forbes, "Strehl ratio as the Fourier transform of a probability density of error differences," Opt. Lett. **41**, 3735–3738 (2017).
42. H. Aryan, K. Liang, M. A. Alonso, and T. J. Suleski, "Predictive models for the Strehl ratio of diamond-machined optics," Appl. Opt. **58**, 3272–3276 (2019).
43. B. D. Strycker, "The Strehl ratio as a phase histogram," Appl. Opt. **62**, 18–24 (2023).
44. A. van den Bos, "A New Method for Synthesis of Low-Peak-Factor Signals," IEEE Trans Acoust. **35**, 120–122 (1987).
45. A. Van Den Bos, "Rayleigh wave-front criterion : comment," J. Opt. Soc. Am. A **16**, 2307-2309 (1999).
46. L. He, C. J. Evans, and A. Davies, "Two-quadrant area structure function analysis for optical surface characterization," Opt. Express **20**, 23275–23280 (2012).
47. L. Mandel and E. Wolf, *Optical Coherence and Quantum Optics* (Cambridge University Press, 1995).
48. C. R. Rao, *Linear Statistical Inference and Its Applications*, 2nd ed. (John Wiley & sons, 1973).

49. B. Efron, *The Jackknife, the Bootstrap and Other Resampling Plans* (Society of Industrial and Applied Mathematics, 1982).

50. R. Zhelem, "Specification of optical surface accuracy using the structure function," Proc. SPIE **8083**, 808310 (2011).

CHAPTER 4: A WORKFLOW FOR MODELING OF GENERALIZED MID-SPATIAL FREQUENCY ERRORS IN OPTICAL SYSTEMS

4.1 Abstract

In this work, we propose a workflow to model generalized mid-spatial frequency (MSF) errors in optical imaging systems. This workflow enables the identification, filtering of bandlimited signatures, propagation of MSF to the exit pupil, and performance prediction that differentiates performance impact due to the MSF distributions. With this workflow, we model the performance impact of MSF for both transmissive and reflective imaging systems that are near diffraction-limited.

4.2 Introduction

Sub-aperture manufacturing of optical components leaves residual mid-spatial frequency (MSF) surface errors as byproducts [1]. MSF errors have spatial frequencies that fall between ‘low frequency’ form and ‘high frequency’ roughness errors, with ambiguous boundaries [2]. MSF errors can have significant detrimental impacts on the optical performance of imaging systems [3–6], which makes robust and widely available modeling procedures and capabilities highly desirable to the optics community. To date, three primary methods have been used for optical modeling of MSF surface errors: (1) statistical transfer functions; (2) perturbation theory; and (3) MSF “phase skins.” We now briefly consider each of these three methods and their capabilities and limitations.

Statistical transfer functions use simple statistical values such as variance and autocorrelation to predict optical performance when multiplied by the optical transfer function (OTF) [7]. Use of statistical transfer functions has evolved from turbulence modeling [8–10] and surface scattering theory [11,12] over multiple decades with similar results under the assumption of random phase screens or random surface errors, respectively. The first use of statistical transfer functions for optical modeling of MSF errors was presented by Noll [13], with similar ideas later presented by Harvey [3]. However, both approaches are limited to MSF error distributions that can be described by Gaussian statistics. This requirement limits the applicability of such methods, as many types of MSF error distributions are highly structured and deterministic, and thus may not follow Gaussian statistics [14–16].

A second modeling method utilizes a combination of perturbation theory [17,18] and statistical optics [10]. Perturbation theory assumes that the amplitude of the perturbations are small and that the directions of the perturbed rays are approximately equal to those of the unperturbed system. Thus, the added optical path lengths from the perturbations are approximately equal to the differences in path lengths between the nominal and perturbed systems [19]. Perturbation theory has previously been used to investigate, for example, the impacts of tilt, displacement, and form errors [17,18]. Youngworth and Stone first proposed the use of perturbation theory to estimate the projection of MSF errors to the exit pupil of an optical system, where the variance of the MSF wavefront error is used to estimate the Strehl ratio [19]. Recent studies have quantified the validity of the perturbative approach for the propagation of MSF to the exit pupil [20,21]. This approach is limited by assumptions that (1) the MSF error distribution within an individual surface is random, and (2) the MSF error distributions on different surfaces in the system are uncorrelated. Consequently, this approach can give misleading results when applied to structured MSF errors with different distributions but the same RMS error statistics [16,22].

Another common modeling approach treats the MSF error like a “phase skin” superimposed onto a nominal surface; the MSF surface error can be thought of as a shallow, conformal grating. This approach has been applied to both synthesized [6,14,15,22–30] and experimentally measured MSF height maps [5,31–33]. While methods to superimpose MSF phase skins onto optical surfaces and apply ray-based or wave-based propagation methods exist within commercial software [5,6,25,26,34,35], previous efforts have largely made one or more of the following limiting assumptions: (1) the modeled optical system consists only of the phase skin superimposed onto a single element at the aperture stop [22,29,31]; (2) the workflow assumed rotationally symmetric or random MSF error distributions [30,32,33]; or (3) the pre-processing of the phase skin does not address the decomposition of MSF errors [5,25,26], which can be of importance because the MSF error may be composed of multiple distributions [36,37].

An additional, recently introduced method uses the Wigner functions to propagate partially coherent light in optical systems containing MSF errors [38]. This approach gives a local description of MSF spatial frequencies at the cost of increasing the dimensionality of the propagation which increases computation time and complexity. To date, only 1D descriptions of MSF errors have been demonstrated with this method [38] and, while the methods provided could be adapted to 2D descriptions, it would further increase the challenges.

With the above modeling approaches, capabilities, and limitations in mind, we now consider desirable features and characteristics of a comprehensive workflow for modeling of MSF errors in optical systems. For example, such a workflow would ideally:

1. Be applicable to generalized MSF error distributions (from completely random to highly structured) without a need to change modeling assumptions [39].
2. Provide the ability to identify characteristic constituent MSF signatures (ie, radial, raster, azimuthal) within complex MSF error distributions [36].
3. Provide an ability to filter and de-couple different constituent signatures and bandlimited spatial frequency ranges from complex MSF error distributions to determine their individual impacts on optical system performance [40,41].
4. Be capable of modeling optical systems with MSF errors using either ray-based [32,33] or wave-based [6,25,34] propagation (as appropriate to balance accuracy and computational load).
5. Generate useful optical performance measures and metrics without assumptions of MSF error distribution geometry or symmetry [16].
6. Leverage commercially available software packages where possible to facilitate broader usage within the optics community [34,35].

In this work, we propose and demonstrate a general workflow with the above capabilities and characteristics. The commercial software packages MATLAB™ and CODE V™ are used for purposes of this demonstration. Section 4.3 presents a high-level overview of the proposed workflow and its implementation within MATLAB™ and CODE V™. In Section 4.4, each step in the workflow is considered in more detail, using a complex experimental MSF error distribution within a transmissive Cooke Triplet system for illustration. In Section 4.5, we demonstrate the application of the workflow to a reflective three-mirror anastigmatic (TMA) telescope system [42] with partially correlated MSF surface errors. Finally, we discuss challenges with the provided methods and propose future applications.

4.3 Overview of Modeling Workflow for MSF Errors

With the desirable characteristics listed above in mind, the proposed workflow starts with a complex MSF distribution that may be a superposition of multiple simpler distributions (e.g., radial and raster). The workflow provided does not make assumptions as to the statistics of the MSF error distributions (i.e., random vs structured) or their symmetry. The commercial software packages MATLAB™ and CODE V™ are widely available and leveraged for this workflow demonstration, but the proposed procedures could be adapted to other packages. This workflow will be of value to optical designers and manufacturers because it enables the features highlighted earlier for an ideal workflow for modeling generalized MSF errors. A summary list of the workflow steps is provided below along with a flow diagram as shown in Figure 4-1.

1. Identification and classification: The first step uses MATLAB™ to identify what MSF error distributions are present over a spatial frequency range by utilizing the polar areal power spectral density (PAPSD) [36,43].
2. MSF error decomposition: With the distributions and relevant bandwidth identified, we use MATLAB™ to fit the MSF surface error with an orthogonal basis set over desired spatial frequency bandlimits. We use the Rapidly Decaying Fourier (RDF) series for demonstration purposes [44,45].
3. Bandlimited filtering of MSF errors: The orthogonal basis then enables bandlimited filtering and de-coupling of specific MSF distributions which enables examination

of individual MSF components from within an otherwise complex MSF distribution [40,41].

(4) Importation of MSF errors into optical software: Complete or filtered MSF error maps are then imported into CODE V™ using an interferogram file [35], and superimposed onto the relevant surface as a phase skin.

(5) Propagation to system exit pupil: In this work, we choose to utilize beam synthesis propagation (BSP) within CODE V™ to propagate MSF errors to the exit pupil [34], but ray-based methods could also be considered in some situations [46].

(6) Calculate exit pupil metrics: We next export the exit pupil phase map to MATLAB™ for analysis. Traditional analysis methods such as determining the wavefront variance or decomposition of the wavefront error into base aberrations can be performed, but in this work we focus on calculating the Pupil Difference Probability Distribution (PDPD) moments and their maxima and demonstrate their use in differentiating between MSF error distributions with otherwise similar statistics [16,39].

(7) Optical performance measures: System performance can be quantified using traditional approaches with, for example the point spread function or 1D modulation transfer function (MTF). In this work we demonstrate use of the PDPD moments and their maxima to estimate optical system performance within CODE V™. This method is not dependent on assumptions regarding MSF error distribution or system symmetry [22,29,39].

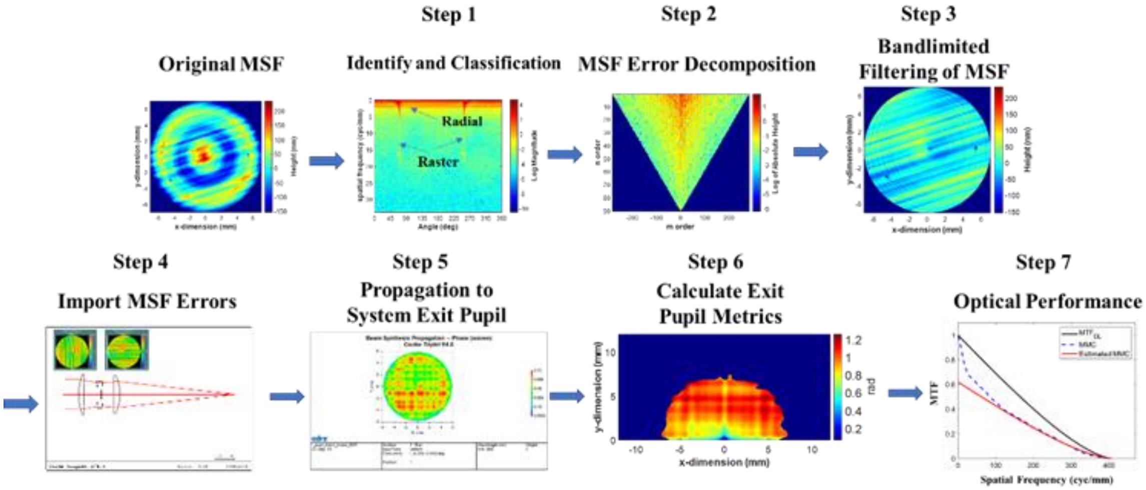

Figure 4-1: Outline of workflow used to model the performance of an optical system with generalized MSF errors.

We note that this workflow as presented assumes an MSF error distribution on a single surface. In cases of systems with MSF error distributions on multiple surfaces, steps 1-4 are repeated for each surface before continuing with step 5 and after. The individual steps in the workflow are considered in more detail and demonstrated for an example refractive optical system in Section 4.4.

4.4 Detailed Workflow Steps and Demonstration with an Example Refractive Optical Systems

4.4.1 Identification and Classification

To characterize MSF distributions, we first window the surface with a circular Blackman window [47]. The Cartesian areal PSD of a circular surface error is calculated using Eq. (4.1) [43]

$$PSD_{Cartesian}(f_x, f_y) = \frac{4}{\pi}\frac{D^2}{(P_x)^2(P_y)^2}\left|H(f_x, f_y)\right|^2, \tag{4.1}$$

where D is the diameter of the surface, P_x and P_y are the number of pixels in the x and y directions, f_x and f_y are the surface spatial frequencies in x and y, and H is the Fourier transform of the surface. The Cartesian areal PSD is then transformed to a polar representation in surface radial spatial frequency (f_r) and angle (θ) that facilitates analysis of the MSF error distribution [36].

Figure 4-2(a) shows a complex MSF distribution with a Peak-Valley (PV) = 388.12 nm and a root mean square error σ = 59.46 nm. The cartesian areal PSD and polar areal PSD of this MSF error distribution are shown in Figures 4-2(b) and 4-2(c) respectively.

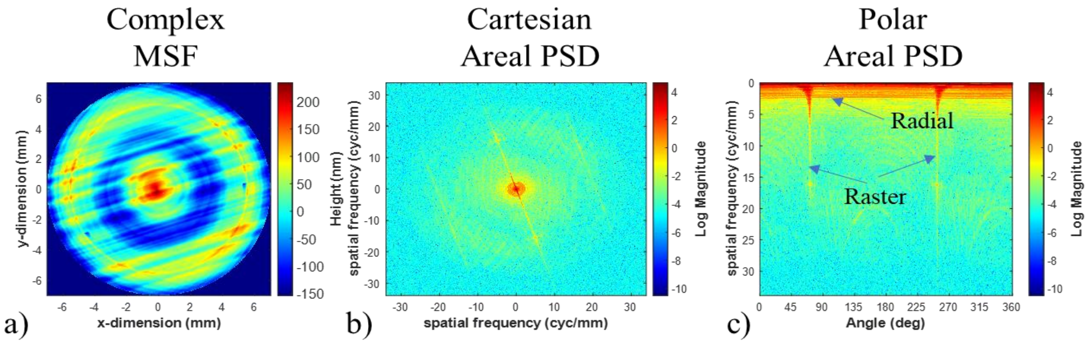

Figure 4-2: (a) Complex MSF error distribution containing both radial and raster MSF signatures. (b) Cartesian areal PSD of this MSF distribution, (c) Polar areal PSD of this MSF distribution. The radial and raster signatures are highlighted.

In Figure 4-2(c), the raster MSF surface errors are observed at 60 deg and 240 deg from approximately 0.1 cyc/mm to 16 cyc/mm. In addition, Figure 4-2(c) shows a radial MSF contribution across all angles from approximately 0.1 cyc/mm to 2.5 cyc/mm. In the MSF error decomposition step in Section 4.4.2, as a demonstration we will focus on the bandlimited raster error component as raster MSF errors tend to have larger performance impacts than radial MSF errors [22].

4.4.2 MSF Error Decomposition

Due to the potential complexity of experimental MSF signatures such as the example shown in Figure 4-2(a), the ability to separate constituent signatures (such as the superimposed raster and radial MSF errors in this example) is desirable. Separation of the signatures enables their impacts on performance to be considered separately, which can facilitate identification and mitigation of the aspect of the manufacturing process giving rise to each constituent pattern. MSF error decomposition splits the overall distribution into a weighted summation of orthogonal polynomials and has previously been demonstrated using several different orthogonal basis sets [31,40,45,48]. The weighting coefficients c_n^m are then placed in a coefficient map as a function of their indices [31,40,49]. In this work, we utilize the $N_b = 1$ solution of the RDF series [44] due to the ability of this basis to define sharp bandlimits [45]. The $N_b = 1$ solution to the RDF is defined in Eqs. (4.2) – (4.4), where Eq. (4.2) describes the weighted sum of the basis, Eq. (4.3) is the radial component, and Eq. (4.4) is the azimuthal component. In Eq. (4.3), R is the surface radius, and α_n^m identifies the zero crossings. In this basis, n is the radial index term and m is the azimuthal index term.

$$\mu(r,\theta) = \sum_{m=-M_{\max}/2}^{M_{\max}/2} \sum_{n=1}^{n=N_{\max}} c_n^m \Re_n^m(r) \psi_m(\theta) , \tag{4.2}$$

$$\Re_n^m(r) = \frac{\sqrt{2} J_m(\alpha_n^m r)}{R\sqrt{J_m^2(\alpha_n^m r) - J_{m-1}^2(\alpha_n^m r)}} , \tag{4.3}$$

$$\psi_m(\theta) = 1/\sqrt{\pi} \begin{cases} 1/\sqrt{2} & m = 0 \\ \cos(m\theta) & m > 0 \\ \sin(|m|\theta) & m < 0 \end{cases} . \tag{4.4}$$

To determine the bandlimited range needed to capture the raster error, we leverage previous work that fitted the whole MSF distribution to a small residual error. In previous work, the polar areal PSD was integrated over f_r and its total angular extent to calculate the contribution to s per number of cycles. At N_c = 90 cycles across the part, σ = 59.36 nm for the surface error, which is within 0.1 nm of the total σ for the surface [45]. Using Eq. (4.5) for D = 14 mm, we can use N_c to determine the corresponding surface radial spatial frequency f_r = 6.42 cyc/mm.

$$f_r = \frac{N_c}{D} \tag{4.5}$$

Therefore, we choose our bandlimited range to be from the lowest resolved spatial frequency of 0.1 cyc/mm to the upper bound of 6.42 cyc/mm to capture the majority of the raster error [47].

To fit up to previously identified upper bandlimit of 6.42 cyc/mm for both radial and raster MSF distributions, we utilize relationships from a previous work that relates the RDF n and m index terms to surface radial spatial frequency f_r, [45]. For the number of n terms, we use the approximation that n is approximately equal to N_c as shown in Eq. (4.6) [45]. The number of m terms can be estimated using the linear relationship between m and n shown in Eq. (4.7) [45].

$$n \approx N_c = Df_r \tag{4.6}$$

$$m \approx \pi n \tag{4.7}$$

The resulting fitting range of $1 \le n \le 90$ and $-283 \le m \le 283$ forms a triangular coefficient map, as shown in Figure 4-3.

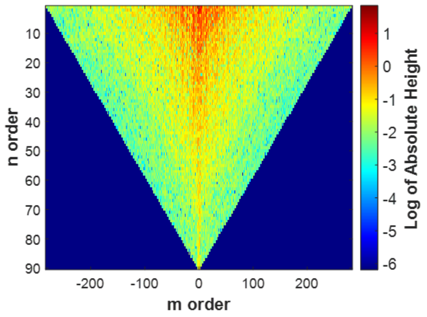

Figure 4-3: RDF coefficient map of surface from Figure 4-2(a)

4.4.3 Bandlimited Filtering of MSF Errors

The raster and radial components in the complex MSF error distributions are separated by subtracting the *m* = 0 column to filter out the radial MSF distribution. Figure 4-4 shows the filtered coefficient map, the filtered height map, and the residual height map calculated by subtracting the filtered height map from the original height map. As can be seen, the filtered MSF surface is majority raster error, and the residual surface is purely radial.

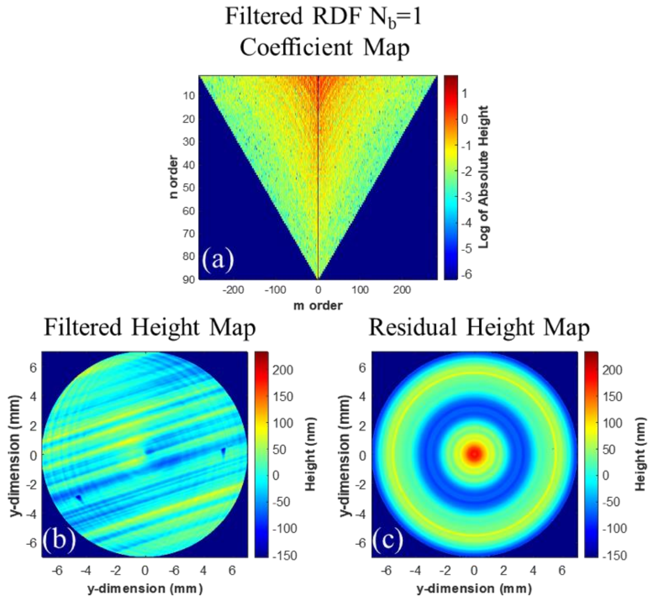
Filtered RDF N_b=1 Coefficient Map

Filtered Height Map

Residual Height Map

Figure 4-4: (a) Filtered RDF N_b = 1 coefficient map, (b) filtered height map, (c) residual height map.

4.4.4 Importation of MSF Errors into Optical Software

The filtering process described above was implemented as a CODE V™ macro that collects user inputs that are then exported as a text file that is passed to MATLAB™. MATLAB™ then runs the filtering calculations and the resulting filtered MSF distribution is saved as an interferogram file that is returned to CODE V™. The interferogram file is then superimposed onto a chosen optical element surface as a surface deformation [35]. The user interface for the macro is shown in Figure 4-5(a), and the surface deformation of the .int file is shown if Figure 4-5(b).

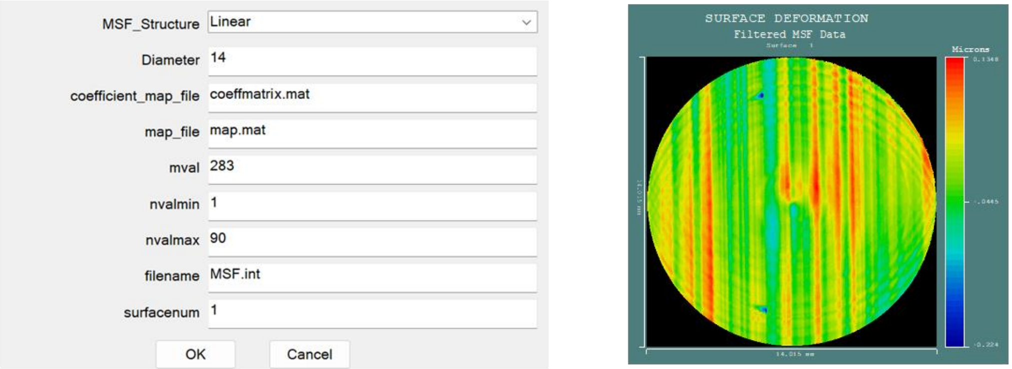

MSF_Structure	Linear
Diameter	14
coefficient_map_file	coeffmatrix.mat
map_file	map.mat
mval	283
nvalmin	1
nvalmax	90
filename	MSF.int
surfacenum	1

(a) (b)

Figure 4-5: (a) Macro user interface, (b) filtered MSF error distribution after import to CODE V™.

As an example, we choose a near-diffraction limited Cooke triplet with on-axis illumination at 546.1 nm, shown in Figure 4-6. Lenses 1 and 3 are made of SK16_SCHOTT glass and lens 2 is made of F4_HOYA glass. The first-order properties of the system were calculated with the FIRABCD macro using matrix multiplication methods [50], as shown in Table 4-1 where all parameters are units of millimeters.

Table 4-1: First order properties of the Cooke triplet example (all units in millimeters).

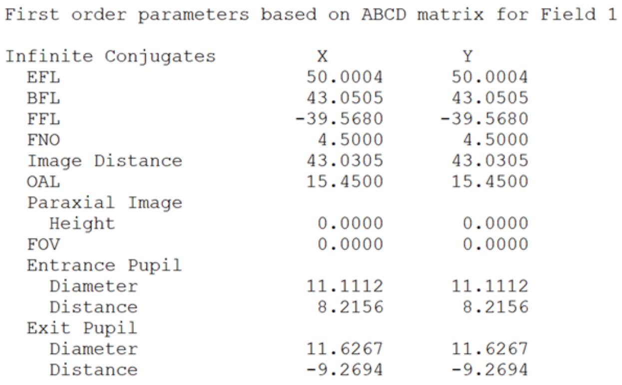

```
First order parameters based on ABCD matrix for Field 1

Infinite Conjugates            X            Y
  EFL                       50.0004      50.0004
  BFL                       43.0505      43.0505
  FFL                      -39.5680     -39.5680
  FNO                        4.5000       4.5000
  Image Distance            43.0305      43.0305
  OAL                       15.4500      15.4500
  Paraxial Image
    Height                   0.0000       0.0000
  FOV                        0.0000       0.0000
  Entrance Pupil
    Diameter                11.1112      11.1112
    Distance                 8.2156       8.2156
  Exit Pupil
    Diameter                11.6267      11.6267
    Distance                -9.2694      -9.2694
```

We then superimposed the bandlimited MSF signature shown in Figure 4-5(b) onto surfaces 1 (S1) and 5 (S5). We modified the amplitude of the MSF signatures by using the ISF command and used the IRO command to scale the orientation [51]. For this example, the MSF signatures on S1 and S5 were rotated to make the orientations perpendicular to each other, and the amplitudes of both MSF signatures were doubled. As shown in Figure 4-6, we also added a dummy surface at the exit pupil of the system with a radius of curvature that matches its distance to the image plane. As discussed in the next section, this curved dummy surface will serve as a reference sphere to remove the nominal curvature of the wavefront in the exit pupil and facilitate quantification of the resulting wavefront error.

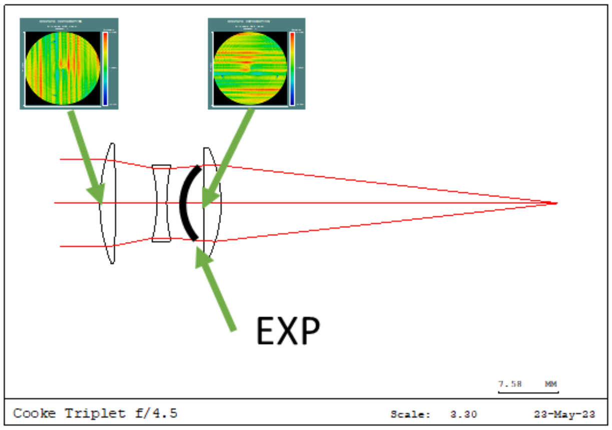

Figure 4-6: MSF surfaces and exit pupil (EXP) dummy surface added to Cooke Triplet.

4.4.5 Propagating to System Exit Pupil

For this demonstration, we use the BSP procedure in CODE V™ to propagate the MSF surface errors in the Cooke triplet to the exit pupil [34]. BSP is a “mixed” model of rays and waves that traces rays with beamlets propagating parallel to the rays. BSP is used because it is compatible with the interferogram files containing the MSF data, and diffraction from the MSF errors is accounted for in the wavefront propagation. However, we note that it may also be possible to use ray-based methods [19,32,33] in some cases, which can reduce computational load and decrease simulation time.

To ensure proper sampling for BSP it is necessary to determine the number of beamlets needed at the entrance of the system. The number of beamlets is dependent on the *number of rings (NRI)* across the aperture used in the initial fit of the field at the system entrance, as shown in Eq. (4.8) [34].

$$\#of\_beamlets = \left[3NRI(1+NRI)+7\right] \tag{4.8}$$

The first step is to find the *NRI* that results in an acceptable wavefront error per beamlet, where less than $\lambda/10$ is ideal [34]. In the current case, this was achieved at $NRI = 90$.

The next step is to check the beamlet width on each surface. The default BSP procedure states that the beamlet width should be less than one-tenth of the aperture of each surface [34]. In the case where MSF errors are considered, the beam width criterion should nominally be sufficient to capture the highest spatial frequency present in the MSF distribution. In the current example, the highest frequency is 6.42 cyc/mm; using the sampling criterion above, this means that the beamlet width on S1 should not exceed 0.16 mm. However, it is also necessary to check the beamlet widths on all the other surfaces. The minimum MSF period for the Nth surface is found by multiplying the MSF period on surface 1 by D_n/D_1, where D_n is the diameter of the N^th^ surface and D_1 is the diameter of the first surface. This approximation assumes that the minimum MSF period is either magnified or demagnified based on the first-order calculations of the system [25]. Table 4-2 summarizes the beamlet maxima half-widths and the minimum MSF period for each surface and shows that *NRI* = 90 provides adequate sampling on all surfaces.

Table 4-2: Summary of minimum MSF period and maximum beamlet width at each surface.

Surface #	Diameter (mm)	Minimum MSF Period (mm)	Max Beamlet Max Width (mm)
1	14.00	0.16	0.08
2	10.88	0.12	0.08
3	8.98	0.11	0.06
4	8.87	0.10	0.06
5	13.00	0.14	0.07
6	9.8	0.11	0.07
7	11.63	0.12	0.08

With the sampling determined, the incident wavefront containing the MSF is propagated through the imaging system and MSF error distributions to the curved dummy surface in the exit pupil (S7) and the phase is calculated and unwrapped [34], as shown in Figure 4-7. The resulting phase distribution is then passed to MATLAB™ as a text file for additional processing, as discussed in more detail in the following section.

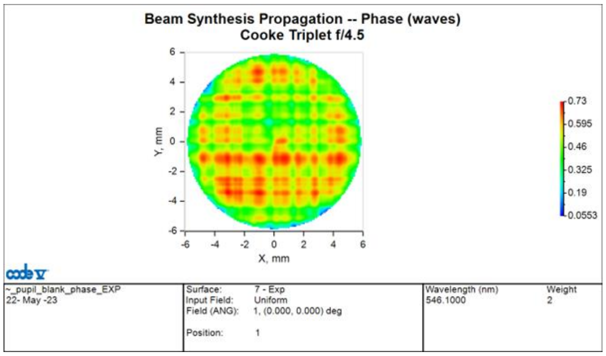

~_pupil_blank_phase_EXP
22- May -23

Surface: 7 - Exp
Input Field: Uniform
Field (ANG): 1, (0.000, 0.000) deg
Position: 1

Wavelength (nm): 546.1000
Weight: 2

Figure 4-7: Exit pupil residual wavefront error for the Cooke triplet example.

4.4.6 Calculation of Exit Pupil Metrics

The wavefront error distribution in the exit pupil of an imaging system serves as the basis for quantifying and understanding the system performance. For example, it is a common procedure to decompose the exit pupil wavefront error distribution into components to understand and quantify astigmatism, coma, distortion, and other fundamental aberrations [52]. It is also common to calculate the variance of the wavefront phase in the exit pupil (σ_{phase}) as a simple, single value metric to quantify the exit pupil wavefront error [19].

We note that the proposed workflow as presented to this point makes no assumptions about the characteristics of the MSF error distributions, so it is still possible to apply the standard methodologies as discussed above. This approach could be quite useful, for example, for better understanding of the impacts of MSF errors on distortion in imaging systems [4,27]. However, as discussed in Section 4.2, the use of simple exit pupil metrics like σ_{phase} can result in misleading predictions of optical performance for systems containing structured MSF error distributions [16,22].

With this limitation in mind, we briefly review our recent work on the use of PDPD moments for analysis of the impacts of generalized MSF error distributions [16,39]. We have previously shown that the 2nd and 4th PDPD moments of and MSF error distribution can be used to predict optical performance for generalized MSF errors [16,39]and are consistent with earlier methods of predicting performance for random surface errors [39].

In Eq. (4.9), W_{dif} is the pupil difference used to calculate the PDPD [14,16], $W(x,y)$ is the exit pupil phase map, x and y are spatial coordinates, and τ_x and τ_y are the pupil shift vectors, which can be related to image space spatial frequency [39].

$$W_{dif}(x,y,\tau_x,\tau_y)=W(x,y)-W(x-\tau_x,y-\tau_y) \tag{4.9}$$

The Nth moments of the PDPD are then calculated from Eq. (4.10):

$$\phi^N(\tau_x,\tau_y)=\frac{\iint[(W_{dif}(x,y,\tau_x,\tau_y)-\overline{W_{dif}(\tau_x,\tau_y)}]^N dxdy}{\iint P_{DL}(x,y)P_{DL}(x-\tau_x,y-\tau_y)dxdy} \tag{4.10}$$

Note, here we have adapted the variables to calculate the PDPD moments of the phase as opposed to the height [16,39]. In Eq. (4.10) P_{DL} is the diffraction limited exit pupil which assumes unit amplitude and zero phase error as in previous work [16,53].

Using the exit pupil phase passed from CODE V™ (Section 4.4.5), the 2nd and 4th PDPD moments are calculated and cropped to 1% normalized standard error in MATLAB™, as shown in Figure 4-8, following the procedures outlined in [16,39].

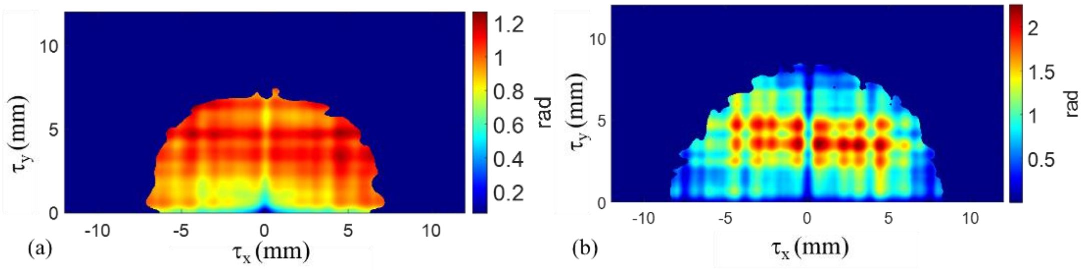

Figure 4-8: Cropped 2nd and 4th PDPD moments of exit pupil phase for Cooke triplet example as a function of pupil shift.

We then find the maxima of the cropped 2nd and 4th PDPD moments for use in the next section for optical performance predictions [39]. The 2nd PDPD moment maxima, ϕ^2_{max}, is 0.90 rad and the 4th PDPD moments maxima, ϕ^4_{maxx}, is 2.25 rad. We note that the maxima units are in radians in this case because the moment maps are calculated from the exit pupil phase instead of surface height as was done in previous work [16,39].

4.4.7 Optical Performance Measures and Metric(s)

A standard method of modeling optical performance is to propagate the wavefront to the image plane and take its modulus squared to get the point spread function (PSF) as shown in Figure 4-9.

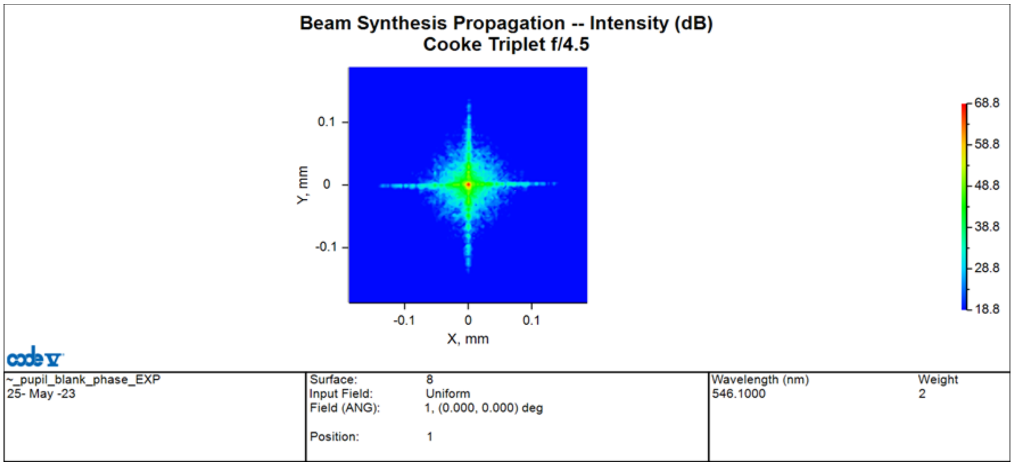

~_pupil_blank_phase_EXP
25- May -23

Surface: 8
Input Field: Uniform
Field (ANG): 1, (0.000, 0.000) deg
Position: 1

Wavelength (nm): 546.1000
Weight: 2

Figure 4-9: PSF of Cooke Triplet example in log scale. Note that the PSF is not radially symmetric due to the presence of the MSF errors on S1 and S5.

One common optical performance measure is the modulation transfer function (MTF), which can be calculated as the modulus of the Fourier transform of the PSF or equivalently as the modulus of the autocorrelation of the exit pupil wavefront [54]. While the 2D MTF contains information about both magnitude and orientation of image contrast as a function spatial frequency, historically it is more common to plot a 1D cross-section of the 2D MTF. This simpler representation is accurate for cases with radial symmetry and/or random MSF error distributions, but can give misleading results in cases with structured error distribution [22]. Similarly, Youngworth and Stone [19] previously showed that, for random MSF error distributions, the Strehl ratio S and the aberrated MTF (MTF_{AB}) can be estimated using σ_{phase} of the exit pupil and the diffraction-limited MTF (MTF_{DL}), as shown in Eqs. (4.11) and (4.12). For the current Cooke triplet example, σ_{phase} = 0.68 rad and S=0.63 from Eq. (4.11):

$$S \approx \exp\left[-(\sigma_{phase}{}^{2})\right] \tag{4.11}$$

$$MTF_{AB} \approx (S)MTF_{DL} \tag{4.12}$$

As discussed in Section 4.2, the assumption of random MSF error distributions can give misleading results when applied to structured MSF errors [16,22]. In previous work our group has reported on additional metrics for quantification of the impacts of structured MSF error distributions, specifically the minimum modulation curve (MMC) [29] and the metric Q' [22] which is analogous to the Strehl ratio. We have recently [39] showed that Q' can be estimated from the maxima of the PDPD moments as shown in Eq. (4.13), and that the MMC can be estimated as shown in Eq. (4.14) [22]. For the current Cooke triplet example, and using the PDPD maxima calculated in Section 4.4.6 with Eq. (4.13), we get Q' = 0.64.

$$Q' \approx 1 - \frac{\phi_{\max}^{2}}{2} + \frac{\phi_{\max}^{4}}{24} \tag{4.13}$$

$$MMC(\rho) \approx Q' MTF_{DL}(\rho) \tag{4.14}$$

A CODE V™ macro was created and used to calculate the minimum modulation curve (MMC) following the procedure from Aryan et al. [29]. The MMC is used in this process because it has been shown to assess the performance impacts of generalized MSF surface errors [22]. For the current Cooke triplet example, Figure 4-10 shows and compares the diffraction-limited MTF with the MMC, the MTF estimated using Eq. (4.12), and the MMC estimated using Eq. (4.14).

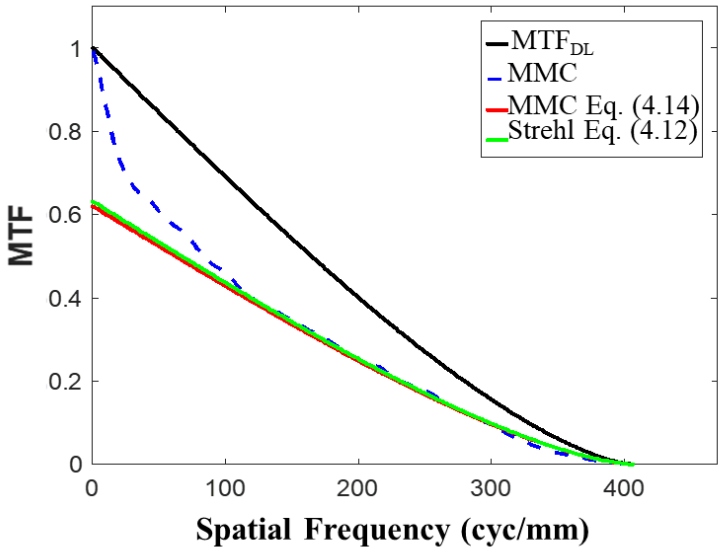

Figure 4-10: Comparing MMC from Cooke Triplet example with performance estimates using Strehl ratio and Q'.

Figure 4-10 shows that use of Q' and Strehl ratio give very similar predictions for the current example. The performance predictors converging to similar values is due to the MSF surface errors being orthogonal, which weakens the correlation of the MSF in the exit pupil. This result is consistent with the assumptions made by Youngworth and Stone [19]. We also note that for the current case, ϕ^2_{max} (0.90 rad) is approximately equal to $2\sigma^2_{phase}$ (0.92 rad). The similarities in performance estimates resulting from Eqs. (4.11)-(4.14) are consistent with earlier analysis that showed equivalence when $\phi^2_{max} = 2\sigma^2_{phase}$ [39]. In our next example, we examine a case where the MSF errors are more correlated which results in a larger variation in the performance predictions.

4.5 Example: Reflective Imaging System with Correlated MSF Errors

In this example we apply the same MSF signature from Section 4.4.4 to a three mirror anistigmat (TMA), [42] shown in Figure 4-11, at $\lambda = 587.56$ nm. We first scale the amplitude of the MSF errors on surfaces S1-S3 by factors of 0.75, 0.5, and 0.5 respectively. We then rotate the MSF signature on S1 and S2 to be orthogonal, and the signature on S3 at 45 degrees relative to S1 and S2. Having this MSF signature at this angle will cause stronger correlations between the three surfaces since the orientation of the MSF errors on the third mirror has components in the *x* and *y* directions that are aligned with the MSF errors on both S1 and S2.

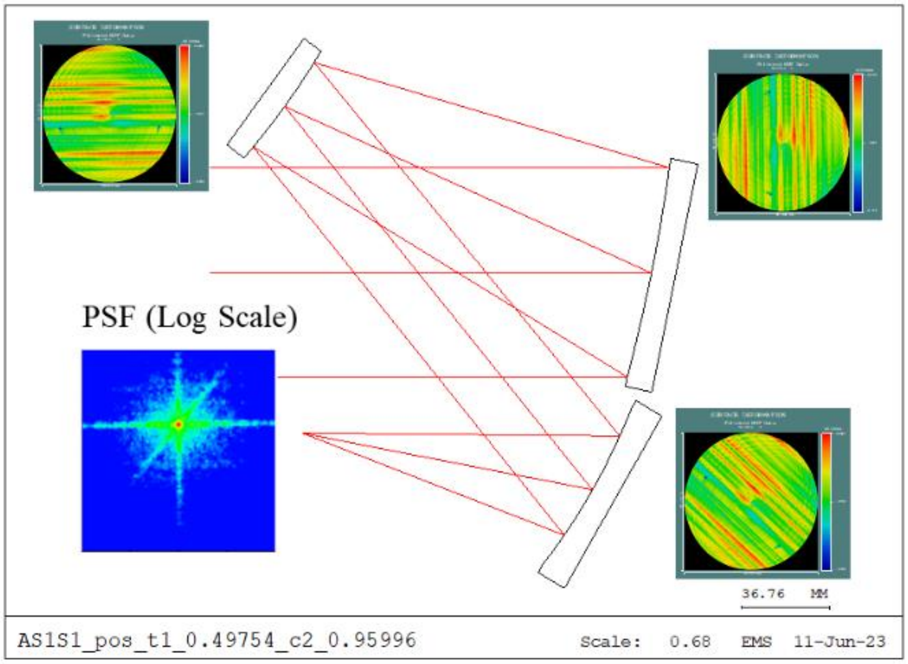

Figure 4-11: TMA example system with partially correlated MSF error distributions.

We applied the previously discussed workflow steps to the example reflective system. It was necessary to increase *NRI* to 110 for the BSP propagation and to tilt the reference sphere to account for tilt present in the exit pupil. The exit pupil residual wavefront error is shown in Figure 4-12(a) and the cropped 2nd and 4th PDPD moments are shown in Figure 4-12(b).

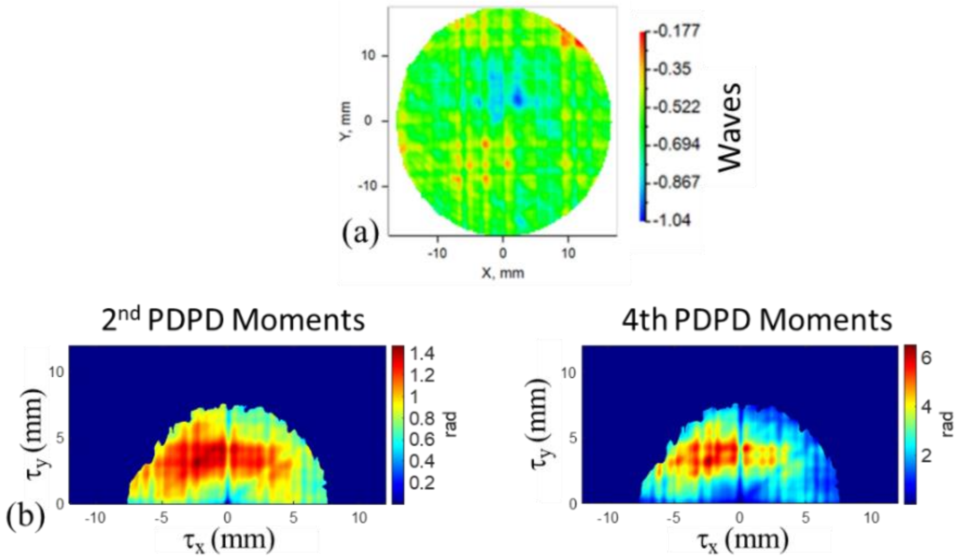

Figure 4-12: For TMA example system; (a) Exit pupil residual wavefront error, (b) cropped 2nd and 4th PDPD moments of exit pupil phase.

The maxima of the 2nd PDPD moment is ϕ^2_{max} = 1.47 rad, the maxima of the 4th PDPD moment is ϕ^4_{max} = 6.50 rad, and σ_{phase} = 0.69 rad. We again utilize Eqs. (4.11) and (4.13) to estimate S = 0.63 and Q' = 0.53, respectively. Eqs. (4.12) and (4.14) are again used to estimate the aberrated MTF and the MMC as shown in Figure 4-13. Compared to the MMC calculated directly for this case, we see that use of Q' (Eq. (4.14)) better estimates the performance. This result is consistent with the observation that ϕ^2_{max} (1.47 rad) is significantly greater than $2\sigma^2_{phase}$ (0.95 rad), which further validates previous results regarding correlated structured MSF errors [39] and demonstrates that when MSF errors from individual surfaces are correlated with one another, the results deviate from predictions that assume uncorrelated errors [19].

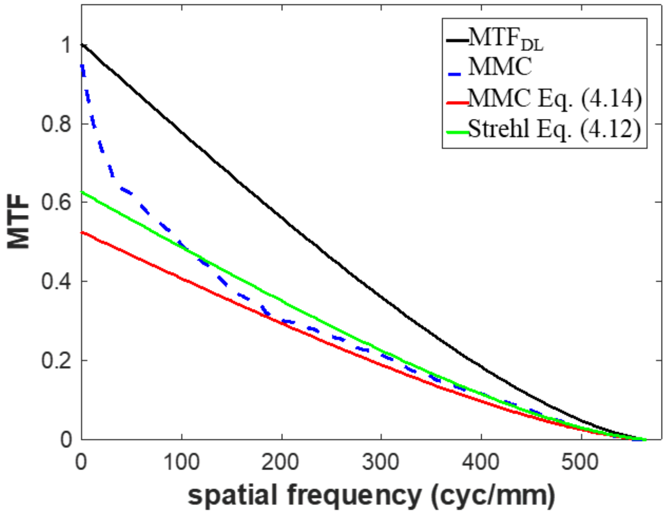

Figure 4-13: Comparing the MMC from the TMA example with performance estimates using Strehl ratio and Q'. For this case with correlated MSF errors, use of Q' provides a better performance estimate than the Strehl ratio.

4.6 Discussion and Conclusions

We have proposed and implemented a workflow for identification, bandlimited filtering, propagation, and prediction of the performance impacts of generalized complex MSF surface errors in optical systems. The proposed procedures do not assume random error distributions as was common in prior work, but instead make use of the PDPD moments of the errors to enable optical performance estimates for both structured and random error distributions. Two presented examples demonstrate the usage and results of the workflow, and also demonstrate how the correlation between MSF errors on different surfaces in the system can impact optical performance predictions. The workflow was demonstrated in MATLAB™ and CODE V™. Implementation using commercial software packages should facilitate accessibility of such procedures to the broader optics community.

Several challenges arise with the added generality of the proposed approach. One challenge is that the procedures for filtering complex bandlimited MSF errors may not always be clear. Raster, azimuthal, and radial MSF error signatures are common, however, there can be MSF distributions that do not fall into these cases. In these scenarios, identifying the patterns in the coefficient maps to isolate the desired distribution using the presented procedures may be challenging. Another challenge is that the PDPD moments themselves can be time-consuming to calculate. However, we note that the maxima of the PDPD moments have the potential to serve as simple ‘single valued’ metrics or acceptance criteria to connect generalized MSF distributions to performance requirements.

Multiple areas of future work are being considered. A key area of interest is exploring the impacts of field dependence when the MSF surface error is far from the exit pupil. Previous work has highlighted that the beam footprint for MSF errors far from the aperture stop can vary greatly as a function of field angle [25]. The proposed methods could be used to explore the field dependencies in greater depth to inform designers and manufacturers how MSF errors over aperture sub-regions may influence performance. We also note that the presented procedures facilitate but do not currently address tolerancing of generalized MSF surface errors. Such a procedure could be realized by varying the amplitude and orientation of bandlimited filtered MSF error distributions, and would allow examination of the sensitivity of different optical systems to particular spatial frequencies and MSF error signatures.

4.7 References

1. J. P. Rolland, M. A. Davies, T. J. Suleski, C. Evans, A. Bauer, J. C. Lambropoulos, and K. Falaggis, "Freeform optics for imaging," Optica **8**, 161–176 (2021).

2. D. M. Aikens, J. E. DeGroote, and R. N. Youngworth, "Specification and control of mid-spatial frequency wavefront errors in optical systems," in Frontiers in Optics 2008/Laser Science XXIV/Plasmonics and Metamaterials/Optical Fabrication and Testing, OSA Technical Digest (CD) paper OTuA1 (2008).
3. J. E. Harvey and A. K. Thompson, "Scattering effects from residual optical fabrication errors," Proc. SPIE **2576**, 155–174 (1995).
4. G. Erdei, G. Szarvas, and E. Lorincz, "Tolerancing surface accuracy of aspheric lenses used for imaging purposes," Proc. SPIE **5249** (2004).
5. J. M. Tamkin and T. D. Milster, "Effects of structured mid-spatial frequency surface errors on image performance," Appl. Opt. **49**, 6522–6536 (2010).
6. V. P. Sivokon and M. D. Thorpe, "Theory of bokeh image structure in camera lenses with an aspheric surface," Opt. Eng. **53**, 065103 (2014).
7. R. Barakat, "The influence of random wavefront errors on the imaging characteristics of an optical system," Opt Acta **18**, 683–694 (1971).
8. R. E. Hufnagel and N. R. Stanley, "Modulation Transfer Function Associated with Image Transmission through Turbulent Media," J. Opt. Soc. Am. **54**, 52 (1964).
9. J. D. Schmidt, *Numerical Simulation of Optical Wave Propagation* (SPIE PRESS, 2010).
10. J. W. Goodman, *Statistical Optics*, 2nd ed. (John Wiley & sons, 2015).
11. E. L. Church and P. Z. Takacs, "Specification of surface figure and finish in terms of system performance," Appl. Opt. **32**, 3344–3353 (1993).
12. J. E. Harvey, "Parametric analysis of the effect of scattered light upon the modulation transfer function," Opt. Eng. **52**, 073110 (2013).

13. R. J. Noll, "Effect of Mid- and High-Spatial Frequencies on Optical Performance," Opt. Eng. **18**, 137–142 (1979).

14. K. Liang and M. A. Alonso, "Understanding the effects of groove structures on the MTF," Opt. Express **25**, 18827–18841 (2017).

15. K. Liang and M. A. Alonso, "Effects on the OTF of MSF structures with random variations," Opt. Express **27**, 34665 (2019).

16. L. A. DeMars and T. J. Suleski, "Pupil-difference moments for estimating relative modulation from general mid-spatial frequency surface errors," Opt. Lett. **48**, 2492–2495 (2023).

17. B. D. Stone and B. D. Stone, "Perturbations of optical systems," J. Opt. Soc. Am. A **14**, 2837–2849 (1997).

18. M. Rimmer, "Analysis of Perturbed Lens Systems," Appl. Opt. Optics **9**, 533–538 (1970).

19. R. N. Youngworth and B. D. Stone, "Simple estimates for the effects of mid-spatial-frequency surface errors on image quality," Appl. Opt. **39**, 2198–2209 (2000).

20. K. Liang, G. W. Forbes, and M. A. Alonso, "Validity of the perturbation model for the propagation of MSF structure in 2D," Opt. Express **27**, 3390–3408 (2019).

21. K. Liang, G. W. Forbes, and M. A. Alonso, "Validity of the perturbation model for the propagation of MSF structures in 3D," Opt. Express **28**, 20277–20295 (2020).

22. H. Aryan, G. D. Boreman, and T. J. Suleski, "Simple methods for estimating the performance and specification of optical components with anisotropic mid-spatial frequency surface errors," Opt. Express **27**, 32709–32721 (2019).

23. W. B. Wetherell, "Effects Of Mirror Surface Ripple On Image Quality," Proc. SPIE **0332**, 335–351 (1982).

24. J. P. Marioge and S. Slansky, "Effect of figure and waviness on image quality," J. Opt. **14**, 189–198 (1983).

25. J. M. Tamkin, W. J. Dallas, and T. D. Milster, "Theory of point-spread function artifacts due to structured mid-spatial frequency surface errors," Appl. Opt. **49**, 4814–4824 (2010).

26. J. M. Tamkin, T. D. Milster, and W. Dallas, "Theory of modulation transfer function artifacts due to mid-spatial-frequency errors and its application to optical tolerancing," Appl. Op. **49**, 4825–4835 (2010).

27. K. Achilles, K. Uhlendorf, and D. Ochse, "Tolerancing the impact of mid-spatial frequency surface errors of lenses on distortion and image homogeneity," Proc. SPIE **9626**, 96260A (2015).

28. H. Aryan, K. Liang, M. A. Alonso, and T. J. Suleski, "Predictive models for the Strehl ratio of diamond-machined optics," Appl. Opt. **58**, 3272–3276 (2019).

29. H. Aryan, G. D. Boreman, and T. J. Suleski, "The Minimum Modulation Curve as a tool for specifying optical performance: application to surfaces with mid-spatial frequency errors," Opt. Express **27**, 25551–25559 (2019).

30. A. Eriksson, "Development of a Software Tool for Mid-Spatial Frequency Analysis," Degree Project, Luleå University of Technology (2021).

31. Z. Hosseinimakarem, A. Davies, and C. J. Evans, "Usefulness of orthogonal basis sets for predicting optical performance of wavefronts with mid-spatial frequency error," Proc. SPIE **10373**, 1037302 (2017).

32. J. Stock, A. Broemel, J. Hartung, D. Ochse, and H. Gross, "Description and reimplementation of real freeform surfaces," Appl. Opt. **56**, 391–396 (2017).
33. J. Stock, M. Beier, J. Hartung, S. Merx, and H. Gross, "Simulation and analysis of optical imaging systems including real freeform components," Adv. Opt. Techn. **8**, 111–117 (2019).
34. Synopsys, *Generalized Beam Propagation and Coupling Efficiency Reference Manual* (2021).
35. Synopsys, *CODE V Lens System Setup Reference Manual* (2021).
36. L. A. DeMars and T. J. Suleski, "Separating and estimating impacts of anisotropic mid-spatial frequency errors," OSA Optical Design and Fabrication 2021 (Flat Optics, Freeform, IODC, OFT), *Paper OW3B.2* (2021).
37. L. A. DeMars, S. Rueda, and T. J. Suleski, "MSFLib: A Data Library of Mid-Spatial Frequency Surface Errors for Optical Modeling and Specification," in Optica Design and Fabrication (IODC, OFT), *Paper OW4B.2* (2023).
38. X. Lu and H. Gross, "Wigner function-based modeling and propagation of partially coherent light in optical systems with scattering surfaces," Opt. Express **29**, 14985–15000 (2021).
39. L. A. DeMars and T. J. Suleski, "On the use of pupil-difference moments for predicting optical performance impacts of generalized MSF surface errors," (In Progress) (n.d.).
40. G. W. Forbes, "Never-ending struggles with mid-spatial frequencies," Proc. SPIE **9525**, 95251B (2015).
41. Z. Hosseinimakarem, A. D. Davies, and C. J. Evans, "Zernike polynomials for mid-spatial frequency representation on optical surfaces," Proc. SPIE **9961,** 99610P (2016).

42. A. Bauer, E. M. Schiesser, and J. P. Rolland, "Starting geometry creation and design method for freeform optics," Nat Commun **9**, 1756 (2018).

43. T. Pertermann, J. Hartung, M. Beier, M. Trost, S. Schröder, S. Risse, R. Eberhardt, A. Tünnermann, and H. Gross, "Angular resolved power spectral density analysis for improving mirror manufacturing," Appl. Opt. **57**, 8692–8698 (2018).

44. K. Liang, G. W. Forbes, and M. A. Alonso, "Rapidly decaying Fourier-like bases," Opt. Express **27**, 32263–32276 (2019).

45. L. A. Demars, S. Rueda, M. A. Alonso, and T. J. Suleski, "Fitting Mid-Spatial Frequency Surface Errors with a Rapidly Decaying Fourier Series," in Optica Design and Fabrication 2023 (IODC, OFT), *Paper OW4B.1* (2023).

46. B. D. Stone and T. J. Bruegge, "Practical considerations for simulating beam propagation: A comparison of three approaches," Proc. SPIE **4832** (2002).

47. Wulang Widada, "Two Dimensional Window Functions," Master Thesis, Naval Postgraduate School (1979).

48. W. Fei, L. Zhao, J. Bai, X. Zhou, J. Hou, H. Yan, and K. Wang, "Feature-based characterization and extraction of ripple errors over the large square aperture," Opt. Express **29**, 8296–8311 (2021).

49. C. J. Evans, R. E. Parks, P. J. Sullivan, and J. S. Taylor, "Visualization of surface figure by the use of Zernike polynomials," Appl. Opt. **34**, 7815–7819 (1995).

50. Synopsys, *CODE V Spec Builder Reference Manual* (2021).

51. Synopsys, *CODE V Prompting Guide* (2021).

52. J. M. Greary, *Introduction to Lens Design with Practical Zemax Examples* (Willman-Bell, 2002).

53. J. W. Goodman, *Introduction to Fourier Optics*, 4th ed. (W.H. Freeman, 2017).

54. G. D. Boreman, *Modulation Transfer Function in Optical and Electro-Optical Systems*, 2nd ed. (SPIE PRESS, 2021).

CHAPTER 5: CONCLUSION

5.1 Summary

In Chapter 2, we reported on the derivation, development, and application of the PDPD moments to specify generalized MSF errors and their connections to the relative modulation without assumption of the stationarity or distribution of the MSF surface error [10,92]. We also demonstrated that the 2nd and 4th PDPD moments can be used to estimate the relative modulation to within 1% for simple MSF structures with symmetric PDPDs. Further, use of the 3rd PDPD moment could enable further analysis of MSF error distributions that produce skewed PDPDs.

Chapter 3 builds on the work in Chapter 2 by demonstrating a procedure using the PDPD moments of the MSF surface errors to predict reductions in optical performance and shown that the 2nd and 4th PDPD can be utilized to estimate the optical performance impacts of both random and deterministic MSF surface errors. In the case of random surface errors, the performance estimates from using the PDPD moments converged to the Strehl ratio, as has been seen using previous methods that assume random MSF error distributions. This convergence occurred when the 2nd PDPD moment maximum was close to its mean. However, we also saw a large variation in optical performance predictions for the range of MSF surface error distributions that were presented. As a result, we believe that it is valuable and necessary to utilize the 2nd and 4th PDPD moment procedures for most cases. Use of PDPD moments as proposed herein enables improved predictions of the impacts of generalized MSF errors on optical performance in imaging systems at the cost of increased calculation complexity.

Chapter 4 demonstrated the integration and application of areal specification tools with MATLAB™ and CODE V™, and a procedure to assess the optical performance impacts of MSF errors in imaging systems using areal tools and a mixed ray-wave diffraction model. We applied our method to both a transmissive Cooke Triplet and a reflective three mirror anastigmatic (TMA) telescope and quantified the performance impacts of MSF errors on multiple surfaces. By modifying the orientation of MSF in these examples, we demonstrated that raster errors that are aligned in angle from one surface to another can result in correlated performance degradation and quantified the performance impacts.

In summary, this work has proposed, demonstrated, and characterized use of the PDPD moments for specifying generalized MSF errors and connecting them to optical performance of optical imaging systems. The PDPD moments enable optical performance predictions for generalized MSF error distributions that distinguish between cases with different distributions but similar statistics, and agrees with previously reported results for cases of random MSF error distributions. This work also identified a workflow that enables specification and performance predictions for generalized MSF errors at a system level and demonstrated its implementation in commercial software packages. This workflow enables performance predictions and modeling of high-performance imaging systems with MSF errors and should be of broad applicability and interest to the optics community.

5.2 Future work

1. As discussed in Chapters 2 and 3, we assumed situations in which the 3rd PDPD moment is negligible. However, the 3rd moment must be considered for MSF errors that cause skewed PDPDs and will add a complex component to the relative

modulation. Such cases should be further explored by expanding on the methods developed within Chapters 2 and 3.

2. We note that the aberrated 2D MTF can be estimated by multiplying the relative modulation (estimated using PDPD moments) by the 2D diffraction-limited MTF. This approach could facilitate definition of optical performance over specific band limits in image space and enable quantification of the performance impacts of MSF errors at targeted image space spatial frequencies.
3. Chapter 4 describes methods that could be used to aid in tolerancing MSF errors in optical systems, but has not yet demonstrated a tolerancing analysis. Multiple builds of bandlimited filtered MSF errors of varying amplitude and orientation could be realized to collect PDPD moments statistics over multiple realizations. Such a procedure would allow examination of the sensitivity of different optical systems to particular spatial frequencies while still enabling distinction of performance impacts due to the MSF distributions.
4. The impacts of off-axis field angles with MSF errors could be explored using the workflow developed in Chapter 4. Increasing the field angle can change the footprint and angle of incidence of the optical beam on a surface, which can result in MSF surface errors that function like different MSF distributions or as form errors [6]. Methods described within Chapter 4 could be extended to estimate these changes in performance as a function of field angle, which would also aid in the tolerancing of MSF errors in optical systems over wider fields of view.
5. A data library (‘MSFLib’) containing a wide range of experimental MSF surface error distributions was developed in collaboration with companies in the Center for

Freeform Optics (CeFO) [12]. This data library could be used with the methods presented in Chapter 4 to further explore the impacts of generalized MSF surface errors on optical performance.

6. We utilized the RDF basis in Chapter 4 to filter MSF surface errors, but have not yet compared this basis to other basis sets such as Zernike [86] and Forbes (2D-Q) [61] polynomials.
7. Previous work [36,75] have suggested that Talbot self-imaging of the MSF surface errors can occur. To date, the ‘rules of thumb’ of self-imaging for experimental MSF errors and how these effects might impact performance predictions have not been rigorously studied. Additional investigation into Talbot image formation from experimental MSF surface errors could be made utilizing the methods in Chapter 4 and surfaces from the MSF data library MSFLib [12].
8. Decomposition of MSF surface errors using an orthogonal basis can be performed at the expense of time and challenges with interpretation of the fitted data. If filtering out particular MSF distributions is the only desired action, it could be beneficial to further explore, for example, rotational averaging of MSF surfaces to filter out azimuthal frequencies associated with raster and azimuthal errors [52,93].
9. The use of experimental surfaces throughout this work has not addressed the impacts that the metrology method and platform might have on measured MSF topography. The presented work determines performance impacts based on the scaled surfaces given from the measurements; further investigations of how metrology methods and platforms may impact the measurement data and subsequent performance predictions from generalized MSF surface errors should be made.

REFERENCES:

1. J. P. Rolland, M. A. Davies, T. J. Suleski, C. Evans, A. Bauer, J. C. Lambropoulos, and K. Falaggis, "Freeform optics for imaging," Optica **8**, 161–176 (2021).
2. D. M. Aikens, J. E. DeGroote, and R. N. Youngworth, "Specification and control of mid-spatial frequency wavefront errors in optical systems," in Frontiers in Optics 2008/Laser Science XXIV/Plasmonics and Metamaterials/Optical Fabrication and Testing, OSA Technical Digest (CD) paper OTuA1 (2008).
3. "ISO 10110 Optics and photonics –Preparation of drawings for optical elements and systems. Part 8: Surface texture; roughness and waviness," (2010).
4. L. L. Deck and C. Evans, "High performance Fizeau and scanning white-light interferometers for mid-spatial frequency optical testing of free-form optics," Proc. SPIE **5921**, 59210A (2005).
5. J. E. Harvey and A. K. Thompson, "Scattering effects from residual optical fabrication errors," Proc. SPIE **2576**, 155–174 (1995).
6. J. M. Tamkin, W. J. Dallas, and T. D. Milster, "Theory of point-spread function artifacts due to structured mid-spatial frequency surface errors," Appl. Opt. **49**, 4814–4824 (2010).
7. J. A. Shultz, M. A. Davies, and T. J. Suleski, "Effects of MSF errors on performance of freeform optics: Comparison of diamond turning and diamond milling," in Imaging and Applied Optics 2015, OSA Technical Digest (online) FT4B.3 (2015).
8. H. Aryan, C. J. Evans, and T. J. Suleski, "On the use of ISO 10110-8 for specification of optical surfaces with mid-spatial frequency errors," Optical Design and Fabrication 2017

(Freeform, IODC, OFT), OSA Technical Digest (online) (Optica Publishing Group, 2017) Part F56-O, paper OW4B.2 (2017).

9. H. Aryan, G. D. Boreman, and T. J. Suleski, "Simple methods for estimating the performance and specification of optical components with anisotropic mid-spatial frequency surface errors," Opt. Express **27**, 32709–32721 (2019).
10. L. A. DeMars and T. J. Suleski, "Pupil-difference moments for estimating relative modulation from general mid-spatial frequency surface errors," Opt. Lett. **48**, 2492–2495 (2023).
11. L. A. DeMars and T. J. Suleski, "Separating and estimating impacts of anisotropic mid-spatial frequency errors," in OSA Optical Design and Fabrication 2021 (Flat Optics, Freeform, IODC, OFT), (Optica Publishing Group, 2021), Paper **OW3B.2.**
12. L. A. DeMars, S. Rueda, and T. J. Suleski, "MSFLib: A Data Library of Mid-Spatial Frequency Surface Errors for Optical Modeling and Specification," in Optica Design and Fabrication (IODC,OFT), Paper **OW4B.2** (2023).
13. S. Rakuff and P. Beaudet, "Thermally induced errors in diamond turning of optical structured surfaces," Opt. Eng. **46**, 103401 (2007).
14. K. Liang and M. A. Alonso, "Effects on the OTF of MSF structures with random variations," Opt. Express **27**, 34665 (2019).
15. A. Sohn, L. Lamonds, and K. Garrard, "MODELING OF VIBRATION IN SINGLE-POINT DIAMOND TURNING," in Proc. ASPE 21st Annual Meeting 15–20 (2006).
16. R. E. Parks and C. J. Evans, "Rapid post-polishing of diamond-turned optics," Precision Eng. **16**, 223–227 (1994).

17. D. Nelson, J. D. Nelson, A. Gould, C. Klinger, and M. Mandina, "Incorporating VIVE into the precision optics manufacturing process," Proc. SPIE **81261**, 812613 (2011).
18. H. Shahinian, M. Hassan, H. Cherukuri, and B. A. Mullany, "Fiber-based tools: material removal and mid-spatial frequency error reduction," Appl. Opt. **56**, 8266–8274 (2017).
19. L. L. Taylor, J. Xu, M. Pomerantz, T. R. Smith, J. C. Lambropoulos, and J. Qiao, "Femtosecond laser polishing of germanium," Opt. Mater. Express **9**, 4165–4177 (2019).
20. G. Chen and J. Qiao, "Femtosecond-laser-enabled simultaneous figuring and finishing of glass with a subnanometer optical surface," Opt. Lett. **47**, 3860–3863 (2022).
21. K. Wan, S. Wan, C. Jiang, C. Wei, and J. Shao, "Sparse bi-step raster path for suppressing the mid-spatial-frequency error by fluid jet polishing," Opt. Express **30**, 6603–6616 (2022).
22. D. D. Walker and C. Dunn, "Pseudo-random tool paths for CNC sub-aperture polishing and other applications," Opt. Express **16**, 18942–18949 (2008).
23. Z. Zhu, X. Zhou, D. Luo, and Q. Liu, "Development of pseudo-random diamond turning method for fabricating freeform optics with scattering homogenization," Opt. Express **21**, 28469–28482 (2013).
24. T. Wang, H. Cheng, W. Zhang, H. Yang, and W. Wu, "Restraint of path effect on optical surface in magnetorheological jet polishing," Appl. Opt. **55**, 935–942 (2016).
25. X. Guo, G. Kim, D. W. Kim, X. Guo, Y. Shu, G. Kim, M. Palmer, H. Choi, and D. W. Kim, "Pseudorandom orbiting stroke for freeform optics postprocessing," Opt. Eng. **58**, 092608 (2019).

26. A. Beaucamp, K. Takizawa, Y. Han, and W. Zhu, "Reduction of mid-spatial frequency errors on aspheric and freeform optics by circular-random path polishing," Opt. Express **29**, 29802–29812 (2021).

27. J. Coniglio, N. Quattrociocchi, M. Eisner, S. Beagley, J. Beck, D. R. Brooks, B. D. Cox, J. Perdue, and J. DeGroote Nelson, "Smoothing mid-spatial frequency (MSF) errors on freeform optics with an algorithm-based robotic platform utilizing deflectometry input," Proc. SPIE **11889**, 118891D (2021).

28. V. S. Negi, T. Wang, H. Garg, W. C. Pullen, X. Ke, S. Kumar RR, H. Choi, U. K. Tiwari, V. Karar, and D. Kim, "Random adaptive tool path for zonal optics fabrication," Opt. Express **30**, 29295–29309 (2022).

29. C. Wang, Y. Han, H. Zhang, C. Liu, L. Jiang, and L. Qian, "Suppression of mid-spatial-frequency waviness by a universal random tree-shaped path in robotic bonnet polishing," Opt. Express **30**, 29216–29233 (2022).

30. J. Coniglio, J. Beck, J. Odle, S. Murty, D. R. Brooks, and J. DeGroote Nelson, "Force controlled mid-spatial frequency error smoothing using machine learning," in Proc. SPIE **12188**, 121880P (2022).

31. Y. Deng, X. Hou, B. Li, J. Wang, and Y. Zhang, "Review on mid - spatial frequency error suppression in optical components manufacturing," Int J Adv Manuf Technol **126**, 4827–4847 (2023).

32. J. M. Tamkin, T. D. Milster, and W. Dallas, "Theory of modulation transfer function artifacts due to mid-spatial-frequency errors and its application to optical tolerancing," Appl. Op. **49**, 4825–4835 (2010).

33. J. P. Marioge and S. Slansky, "Effect of figure and waviness on image quality," J. Opt. **14**, 189–198 (1983).

34. J. M. Tamkin and T. D. Milster, "Effects of structured mid-spatial frequency surface errors on image performance," Appl. Opt. **49**, 6522–6536 (2010).

35. X. Lu and H. Gross, "Wigner function-based modeling and propagation of partially coherent light in optical systems with scattering surfaces," Opt. Express **29**, 14985–15000 (2021).

36. V. P. Sivokon and M. D. Thorpe, "Theory of bokeh image structure in camera lenses with an aspheric surface," Opt. Eng. **53**, 065103 (2014).

37. K. Liang, G. W. Forbes, and M. A. Alonso, "Validity of the perturbation model for the propagation of MSF structures in 3D," Opt. Express **28**, 20277–20295 (2020).

38. G. Erdei, G. Szarvas, and E. Lorincz, "Tolerancing surface accuracy of aspheric lenses used for imaging purposes," Proc. SPIE **5249** (2004).

39. K. Achilles, K. Uhlendorf, and D. Ochse, "Tolerancing the impact of mid-spatial frequency surface errors of lenses on distortion and image homogeneity," Proc. SPIE **9626**, 96260A (2015).

40. J. A. Cole, J. A. Cuadra, R. M. Panas, and S. T. Smith, "The effect of longer-range waviness on X-ray reflectivity measurements," J. of Synchrotron Rad., 71–77 (2021).

41. R. J. Noll, "Effect of Mid- and High-Spatial Frequencies on Optical Performance," Opt. Eng. **18**, 137–142 (1979).

42. R. N. Youngworth and B. D. Stone, "Simple estimates for the effects of mid-spatial-frequency surface errors on image quality," Appl. Opt. **39**, 2198–2209 (2000).

43. T. Suleski, "Freeform optics for Imaging: Mid-Spatial Frequency Errors," https://www.photonics.com/Webinars/Freeform_Optics_for_Imaging_Mid-Spatial/w406.

44. Synopsys, CODE V Diffraction Analysis Reference Manual (2021).

45. R. Zhelem, "Specification of optical surface accuracy using the structure function," Proc. SPIE **8083**, 808310 (2011).

46. Z. Ren, C. Gao, D. Luo, and B. Gao, "Intermediate-frequency error identification of precision optical surface based on the Hilbert spectrum and instantaneous frequency filtering method," Opt. Eng. **57**, 064108 (2018).

47. R. N. Youngworth, B. B. Gallagher, and B. L. Stamper, "An overview of power spectral density (PSD) calculations," in Proc. SPIE **5869**, 58690U (2005).

48. W. Fei, L. Zhao, J. Bai, J. Hou, H. Yan, and K. Wang, "Two characterization methods of ripple errors for the large square aperture," Appl. Opt. **60**, 8706–8715 (2021).

49. A. Corunin, "Q-Spectrum and its application for the characterization of mid-spatial frequencies on polished surfaces," Appl. Opt. **57**, 5314–5218 (2018).

50. T. Pertermann, J. Hartung, M. Beier, M. Trost, S. Schröder, S. Risse, R. Eberhardt, A. Tünnermann, and H. Gross, "Angular resolved power spectral density analysis for improving mirror manufacturing," Appl. Opt. **57**, 8692–8698 (2018).

51. T. Lammers, M. Beier, J. Hartung, and H. Gross, "Analysis of mid-spatial frequency errors in two dimensions at metal mirror fabrication," Proc. SPIE **11175**, 111751E (2019).

52. S. Reichelt, "Decomposition of non-rotationally symmetric wavefront aberrations into their azimuthal orders," Proc. SPIE **11102**, 111020B (2019).

53. Y. Sekman, M. Trost, T. Lammers, J. Hartung, S. Risse, and S. Schröder, "Topography stitching in the spatial frequency domain for the representation of mid-spatial frequency errors," Appl. Opt. **61**, 8286–8301 (2022).

54. J. M. Elson and J. M. Bennett, "Calculation of the power spectral density from surface profile data," Appl. Opt. **34**, 201–208 (1995).

55. E. L. Church, A. Jenkinson, and J. M. Zavada, "Relationship between Surface Scattering and Micro topographic Features," Opt. Eng. **18**, 125–136 (1979).

56. F. Tinker and K. Xin, "Correlation of mid-spatial features to image performance in aspheric mirrors," Proc. SPIE **8837**, 88370N (2013).

57. J. R. Rogers, "Surface slope error tolerances: Applicable range of spatial frequencies," in OSA Optical Design and Fabrication 2021 (Flat Optics, Freeform, IODC, OFT) (Optica Publishing Group (formerly OSA), 2021).

58. C. J. Evans, R. E. Parks, P. J. Sullivan, and J. S. Taylor, "Visualization of surface figure by the use of Zernike polynomials," Appl. Opt. **34**, 7815–7819 (1995).

59. Z. Hosseinimakarem, A. D. Davies, and C. J. Evans, "Zernike polynomials for mid-spatial frequency representation on optical surfaces," Proc. SPIE **9961**, 99610P (2016).

60. L. A. DeMars, S. Rueda Parra, M. A. Alonso, and T. J. Suleski, "Fitting Mid-Spatial Frequency Surface Errors with a Rapidly Decaying Fourier Series," in Optica Design and Fabrication (IODC,OFT), Paper **OW4B.1** (2023)

61. G. W. Forbes, "Never-ending struggles with mid-spatial frequencies," Proc. SPIE **9525**, 95251B (2015).

62. W. Fei, L. Zhao, J. Bai, X. Zhou, J. Hou, H. Yan, and K. Wang, "Feature-based characterization and extraction of ripple errors over the large square aperture," Opt. Express **29**, 8296–8311 (2021).

63. M. Maksimovic, "Optical tolerancing of structured mid-spatial frequency errors on free-form surfaces using anisotropic radial basis functions," Proc. SPIE **9626**, 962613 (2015).

64. J. Stock, M. Beier, J. Hartung, S. Merx, and H. Gross, "Simulation and analysis of optical imaging systems including real freeform components," Adv. Opt. Techn. **8**, 111–117 (2019).

65. X. Zhou, X. Huang, J. Bai, L. Zhao, J. Hou, K. Wang, and Y. Hua, "Representation of complex optical surfaces with adaptive radial basis functions," Appl. Opt. **58**, 3938–3944 (2019).

66. G. M. Marshall, "Orthogonal mode decomposition of aspheric surface form errors by principal components analysis," Opt. Eng. **57**, 124103 (2018).

67. L. He, C. J. Evans, and A. Davies, "Two-quadrant area structure function analysis for optical surface characterization," Opt. Express **20**, 23275–23280 (2012).

68. D. L. Fried, "Statistics of a Geometric Representation of Wave-front Distortion," J. Opt. Soc. Am. **55**, 1427–1435 (1965).

69. L. He, C. J. Evans, and A. Davies, "Optical surface characterization with the area structure function," CIRP Ann Manuf Technol **62**, 539–542 (2013).

70. K. Liang and M. A. Alonso, "Understanding the effects of groove structures on the MTF," Opt. Express **25**, 18827–18841 (2017).

71. M. Rimmer, "Analysis of Perturbed Lens Systems," Appl. Opt. **9**, 533–538 (1970).

72. B. D. Stone and B. D. Stone, "Perturbations of optical systems," J. Opt. Soc. Am. A **14**, 2837–2849 (1997).

73. J. W. Goodman, *Statistical Optics*, 2nd ed. (John Wiley & sons, 2015).

74. K. Liang, G. W. Forbes, and M. A. Alonso, "Validity of the perturbation model for the propagation of MSF structure in 2D," Opt. Express **27**, 3390–3408 (2019).

75. K. Liang, G. W. Forbes, and M. A. Alonso, "The validity of the perturbation model for the propagation of MSF structures in 3D," Opt. Express **28**, 20277–20295 (2020).

76. R. Barakat, "The influence of random wavefront errors on the imaging characteristics of an optical system," Opt Acta **18**, 683–694 (1971).

77. R. E. Hufnagel and N. R. Stanley, "Modulation Transfer Function Associated with Image Transmission through Turbulent Media," J Opt Soc Am **54**, 52 (1964).

78. J. D. Schmidt, *Numerical Simulation of Optical Wave Propagation* (SPIE PRESS, 2010).

79. E. L. Church and P. Z. Takacs, "Specification of surface figure and finish in terms of system performance," Appl. Opt. **32**, 3344–3353 (1993).

80. J. E. Harvey, "Parametric analysis of the effect of scattered light upon the modulation transfer function," Opt. Eng. **52**, 073110 (2013).

81. J. E. Harvey, "The surface PSD and image degradation due to mid-spatial-frequency errors," Proc. SPIE **11813**, 118130O (2021).

82. W. B. Wetherell, "Effects Of Mirror Surface Ripple On Image Quality," Proc. SPIE **0332**, 335–351 (1982).

83. H. Aryan, K. Liang, M. A. Alonso, and T. J. Suleski, "Predictive models for the Strehl ratio of diamond-machined optics," Appl. Opt. **58**, 3272–3276 (2019).

84. A. Eriksson, "Development of a Software Tool for Mid-Spatial Frequency Analysis," Degree Project, Luleå University of Technology (2021).

85. M. Maksimovic, "Optical design and tolerancing of freeform surfaces using anisotropic radial basis functions," Opt. Eng. **55**, 071203 (2016).

86. Z. Hosseinimakarem, A. Davies, and C. J. Evans, "Usefulness of orthogonal basis sets for predicting optical performance of wavefronts with mid-spatial frequency error," Proc. SPIE 10373, 1037302 (2017).

87. J. Stock, A. Broemel, J. Hartung, D. Ochse, and H. Gross, "Description and reimplementation of real freeform surfaces," Appl. Opt. **56**, 391–396 (2017).

88. H. Aryan, G. D. Boreman, and T. J. Suleski, "The Minimum Modulation Curve as a tool for specifying optical performance: application to surfaces with mid-spatial frequency errors," Opt. Express **27**, 25551–25559 (2019).

89. H. Aryan, G. D. Boreman, and T. J. Suleski, "Simple methods for estimating the performance and specification of optical components with anisotropic mid-spatial frequency surface errors," Opt. Express **27**, 32709–32721 (2019).

90. Synopsys, CODE V Lens System Setup Reference Manual (2021).

91. Synopsys, Generalized Beam Propagation and Coupling Efficiency Reference Manual (2021).

92. E. Wolf, *Introduction to the Theory of Coherence and Polarization of* Light (Cambridge University Press, 2007).

93. C. J. Evans and R. N. Kestner, "Test optics error removal," Appl. Opt. **35**, 1015–1021 (1996).